

1 **Revision 1**

2 **Trona at extreme conditions: A pollutant-sequestering material at high pressures and low**
3 **temperatures**

4 **Earl O'Bannon III,^{1*} Christine M. Beavers,^{1,2} and Quentin Williams¹**

5 ¹Department of Earth and Planetary Sciences, University of California, Santa Cruz, 1156 High
6 Street, Santa Cruz, California 95064, U.S.A.

7 ²Advanced Light Source, Lawrence Berkeley National Laboratory, Berkeley, California, 94720,
8 U.S.A.

9 **Abstract**

10 Single crystal X-ray diffraction of trona, $\text{Na}_3\text{CO}_3\text{HCO}_3 \cdot 2\text{H}_2\text{O}$, was measured between
11 100 and 340 K at ambient pressures, and the infrared and Raman spectra of this material
12 characterized to ~25 GPa. The thermal expansion of trona is greatest in the *b* direction, which is
13 due to a particularly large expansion of the long $\text{Na}_2\text{-O}_1$ and the short $\text{Na}_2\text{-O}_4$ bonds within the
14 sodium septahedron in the trona structure. This crystallographic direction is associated with the
15 distance between neighboring carbonate groups and neighboring water molecules within the
16 structure. The dimensions of the carbonate group undergo no systematic changes over this
17 temperature range, and the disordered hydrogen atom within the structure does not order at
18 temperatures down to 100 K. Thus, detailed changes in the geometry of the sodium polyhedra
19 primarily modulate the response of trona to decreases in temperature. The infrared and Raman
20 spectra undergo discontinuous and reversible changes at ~7 GPa and ~14.5 GPa: the former of
21 these phase transitions is likely associated with a shift primarily in the sodium-oxygen polyhedra,
22 while the latter also involves shifts in bonding of the carbonate groups. New assignments are
23 suggested for portions of the vibrational spectrum based on the high-pressure results. Resonance

24 effects between different vibrational modes are observed, including the observation of a
25 transmission maximum associated with a resonant interaction between the carbonate symmetric
26 stretching vibration and a broad mode at similar frequencies. The behavior of trona under
27 extreme conditions is useful for understanding CO₂-vapor-saturated alkali-rich systems, and late-
28 stage peralkaline magmatic processes and, in its usage as both a sorbent and scrubber of SO₂ and
29 CO₂ in flue gasses and lignite coals.

30

31 Keyword: trona, high pressure, low temperature, single crystal diffraction, vibrational
32 spectroscopy

33

Introduction

34 Trona, Na₃CO₃HCO₃•2H₂O, is a non-marine evaporite mineral that, from the perspective
35 of its chemical formula, contains the unusual combination of both a carbonate and bicarbonate
36 anion. It has environmental importance as a product of carbon sequestration of flue gasses (Yoo
37 et al. 2013; Ficicilar and Dogu 2006) and in its utilization in sulfur removal from both flue gasses
38 and lignite coals (Kong and Wood 2010; Su et al. 2011; Sutcu and Eker 2013). Additional uses
39 of trona include as a food additive (Nielsen, 1999; Ekosse, 2010), and as a common source of
40 soda ash, which is a significant economic commodity because of its applications in
41 manufacturing glass, chemicals, paper, detergents, and textiles. Trona is also observed as a phase
42 within deteriorating concrete (Figg et al. 1976). Hence, the properties of trona at differing
43 conditions of pressure and temperature can provide insights into the interplay between the
44 structure and stability of this phase. From a crystal chemical viewpoint, trona is of interest as a
45 carbonated phase that contains both water and hydroxyl units, and hence may provide insights
46 into how water and carbonate ions interact within a single phase: indeed, its response to pressure

47 may provide insight into the structural changes undergone by salt-bearing carbon-rich aqueous
48 fluids and/or hydrated carbonatitic magmas under compression.

49 Trona has also been found in magmatic environments: Markl and Baumgartner (2002)
50 show that trona can be formed by autometasomatic reactions of late-magmatic fluids or melts (or
51 supercritical fluid-melt mixtures), with earlier crystallized rocks within the same plutonic
52 complex, or by large-scale vapor unmixing in the very final stages of magmatism. Furthermore,
53 Liu and Fleet (2009) have found that trona's thermal stability is markedly enhanced by pressures
54 of only a few tenths of a GPa: at ambient pressure, trona begins to decompose at ~340 K, but Liu
55 and Fleet (2009) observed it to be stable up to 848 K at 0.21 GPa in equilibrium with CO₂-rich
56 vapor. Thus, understanding the behavior of trona under extreme conditions is useful for
57 understanding late-stage peralkaline magmatic processes, and CO₂-vapor-saturated alkali-rich
58 systems.

59 Brown et al. (1949) first determined the crystal structure of trona using single crystal x-
60 ray diffraction. Bacon and Curry (1956) refined the structure with two-dimensional single-crystal
61 neutron diffraction, and suggested that the H atom in the symmetric (HC₂O₆)³⁻ anion is
62 disordered. This disordering of the hydrogen generates a sharing of the hydrogen atom between
63 the carbonate units, and hence produces the mixed carbonate/bicarbonate character of these
64 anion groups. Candlin (1956) refined the structure at both low (103 K) and room temperature
65 using two-dimensional X-ray diffraction, which confined the data to thermal changes within the
66 (010) plane of the trona structure. The results suggested that six of the twelve Na-O nearest
67 neighbor distances measured at 103 K were larger than at ambient conditions, implying that the
68 thermal response of the Na-O polyhedra may be complex. The environment of the disordered H
69 atom was later investigated by Choi and Mighell (1982) at 300 K with three-dimensional single-

70 crystal neutron diffraction: they concluded that the H atom is dynamically disordered between
71 two equivalent sites, separated from one another by 0.211(9) Å. The dynamically disordered H-
72 atom was later reinvestigated by Pertlik (1986) with single crystal x-ray diffraction and
73 determined it to be separated by 0.95(4) Å to 0.77(3) Å.

74 From a spectroscopic viewpoint, trona has attracted interest as an example of a phase
75 with weak- to medium strength hydrogen bonds, which displays a variety of resonance-related
76 phenomena, including having an anomalous sharp transmission *maximum* within its infrared
77 spectrum (Novak et al. 1963; Bertoluzza et al. 1981). Additionally, its far-infrared spectrum has
78 recently been characterized as an example of a hydrated acid carbonate (Brusentsova et al. 2010).
79 The response, and stability, of carbonates under pressure utilizing vibrational spectroscopy has
80 been a topic of widespread interest (e.g., Kraft et al. 1991; Biellman et al. 1993; Catalli and
81 Williams 2005; Lin et al. 2012; Palaich et al. 2013). In the instance of trona, we examine the
82 effect of a markedly different chemical environment on the stability of the carbonate unit under
83 pressure: a phase that incorporates the bicarbonate ion and abundant water, and hence is a
84 crystallographic representative of the well-known carbonate-bicarbonate equilibrium.

85 Hence, because of its interest as both an industrial material and its novel crystal
86 chemistry, we have examined trona at temperatures spanning most of its ambient pressure
87 stability range (100 K-340 K), and at high pressures. Trona was reinvestigated with single crystal
88 x-ray diffraction techniques at low and ambient temperature to: (1) improve our understanding of
89 the thermal response of this material at a range of temperatures below the onset of its
90 decomposition at ~340 K (e.g., Cho et al. 2008); and (2) to assess the results of Candlin (1956) in
91 which she calculated that some Na-O bonds anomalously contract with increasing temperature.
92 Correspondingly, we have measured the infrared and Raman spectrum of this phase at high

93 pressures, extending up to ~25 GPa to: (1) examine whether pressure-induced polymorphism
94 occurs in this phase; (2) probe how the bonding of this carbonate/bicarbonate/water-bearing
95 phase shifts as a function of compression and particularly how the hydrogen bonding in this
96 phase changes; (3) investigate the behavior of resonant interactions within this phase under
97 compression; and (4) to constrain how the sodium polyhedra (which comprise both octahedral
98 and septahedral sites) might respond to compression. Our net goals are to gain insights into the
99 underlying cause of trona's low-pressure, modest temperature decomposition, and its stability or
100 metastability under high-pressure conditions.

101 **Experimental methods**

102 **Single-crystal structural refinement**

103 The specimen studied is from the Green River Basin in Wyoming and contained
104 columnar, optical quality crystals of trona. The sample identity was confirmed by x-ray
105 diffraction, and both Raman and infrared spectroscopy (Figure 1). Indeed, our spectroscopic
106 results are in excellent accord with prior results on synthetic samples (Novak et al. 1963;
107 Bertoluzza et al. 1981).

108 For low- and ambient-temperature measurements, a single crystal was prepared with
109 approximate dimensions of 0.02 x 0.02 x 0.03 mm, which was mounted in oil (Infineum V8512)
110 on a MiTeGen MicroMount. Data were collected at 100 K, 200 K, and 300 K on a Bruker
111 diffractometer equipped with a Cu-K α I μ S source and MX optic with an APEX-II CCD detector.
112 The sample was placed in a cooled liquid nitrogen stream provided by an Oxford Cryosystems
113 Cryostream 700 liquid nitrogen-cooling device, with a temperature accuracy of ± 2 K. An
114 approximate half sphere of data to $2\theta_{\max}=135.9^\circ$ was collected using 0.5° ω and Φ scans.

115 The higher temperature single-crystal data were collected at 320 K, 330 K, and 340 K.
116 The sample was placed into a warmed nitrogen stream provided by an Oxford Cryosystems
117 Cryostream 700 Plus low/high temperature apparatus, again with an accuracy of ± 2 K. A Bruker
118 D8 diffractometer equipped with an ApexII CCD detector on beamline 11.3.1 at the Advanced
119 Light Source in Berkeley, CA was used. Diffraction data were collected using monochromatic
120 synchrotron radiation at a wavelength of 0.61990(1) Å. An approximate full sphere of data to 2θ
121 $_{\max}=64^\circ$ was collected using 0.3° ω scans.

122 The data were integrated using the program SAINT v8.27B. A multi-scan correction for
123 absorption was applied using the program SADABS-2012/1 and TWINABS-2012/1, for high
124 temperatures and low temperatures, respectively. The structure was solved by the charge flipping
125 methods of OLEX 2 (Dolomanov et al., 2009) and refined by full-matrix least-squares on F^2
126 SHELXL-2013 (Sheldrick, 2008).

127 **High pressure techniques**

128 High static pressures were generated by a Merrill-Basset type diamond anvil cell (DAC)
129 equipped with type Ia diamonds with 500 μm 16-sided culets. An inconel gasket with a 200 μm
130 hole was used as the sample compartment. Three to five ruby chips were loaded with each
131 sample to measure the pressure using the standard ruby fluorescence method (Mao et al., 1986).
132 All experiments were conducted at room temperature.

133 **Raman Spectroscopy**

134 Raman spectra were collected with a Horiba LabRAM HR Evolution Raman
135 spectrometer with a spectrometer focal length of 800 mm. Spectra were collected to a pressure of
136 25 GPa at 300 K. An excitation wavelength of 633 nm was used to collect spectra from 50-350
137 cm^{-1} , while 532 nm excitation was used to collect from 500-1200 cm^{-1} . An Olympus BXFM-

138 ILHS microscope with a 50x long working distance objective (18 mm working distance and 3.6
139 mm focal distance) was used to focus the laser beam onto the sample. An 1800 lines/mm grating
140 with a corresponding spectral resolution of $\sim 1 \text{ cm}^{-1}$ was utilized. A single crystal of trona was
141 loaded with spectroscopic-grade KBr as the pressure medium: since KBr has no first-order
142 Raman spectrum, no spectral contamination of the trona spectrum is generated, and there is no
143 interaction between the pressure medium and the trona sample. Spectra were collected from a
144 laser spot size of $\sim 2 \text{ }\mu\text{m}$, so we do not anticipate that pressure gradients will notably adversely
145 affect our spectra. Multiple samples were run with the trona loaded into the cell in different
146 orientations, so the amplitudes of peaks shift between different runs, due to the orientation-
147 dependence of the Raman modes of trona. Raman spectra were fit using a combination of
148 Gaussian and Lorentzian functions with Horiba LabSpec6 software.

149 **Infrared spectroscopy**

150 Mid-infrared absorbance spectra were collected from 0 to 24 GPa using a Bruker Vertex
151 70v evacuated Fourier transform infrared spectrometer (FTIR) equipped with a globar source,
152 KBr-beamsplitter and a liquid-N₂ cooled mercury-cadmium-telluride (MCT) detector. All
153 infrared spectra were collected with a resolution of 4 cm^{-1} . Trona was ground into a powder and
154 mixed with spectroscopic-grade KBr in a ratio of 90% KBr: 10% sample by weight, with KBr
155 serving as both an infrared window and the pressure medium. Infrared spectra were fit using a
156 combination of Gaussian and Lorentzian functions with Bruker OPUS6.5 software.

157 **Single-Crystal Diffraction Results**

158 Trona crystallizes in the monoclinic C2/c crystal system in the range between 100-340 K
159 (Figure 2). The architecture of the structure is comprised of units of 3 edge-sharing sodium
160 polyhedra (a central octahedron flanked by septahedra), cross-linked by carbonate groups and

161 hydrogen bonds. The unit cell dimensions as a function of temperature are given in Table 1, and
162 the volume as a function of temperature in Figure 3. The high temperature data are somewhat
163 scattered, and we do not preclude that this scatter may be associated with behavior precursory to
164 trona decomposition, which has been observed to initiate, with a substantial kinetic impediment,
165 at temperatures as low as 330 K (Cho et al. 2008). Indeed, our sample lost its single crystal
166 character on heating to 350 K. The average thermal expansion is $7.81 (\pm 0.52) \times 10^{-5}/\text{K}$ over this
167 temperature range. This is at the lower end of the range of other water-bearing molecular
168 minerals with comparatively low decomposition temperatures, such as gypsum ($8.2 \times 10^{-5}/\text{K}$:
169 Ballirano and Melis 2009), mirabilite ($\sim 11 \times 10^{-5}/\text{K}$ at 300 K: Brand et al. 2009) and ikaite (~ 12
170 $\times 10^{-5}/\text{K}$: Lennie et al. 2004). The modulated structure of $\gamma\text{-Na}_2\text{CO}_3$ has, for comparison, an
171 anomalously high thermal expansion over this temperature range of $\sim 14.6 \times 10^{-5}/\text{K}$ (Arakcheeva
172 et al. 2010). Yet, the thermal expansion of trona is dramatically greater than that of non-alkali,
173 and non-water-bearing phases such as, for example, calcite at 300 K ($3.8 \times 10^{-6}/\text{K}$: Markgraf and
174 Reeder 1985).

175 The normalized a and c axes have similar linear thermal expansion values with increasing
176 temperature, whereas the b axis linear thermal expansion is higher by a factor of three (Figure 4).
177 For each temperature the fractional atomic coordinates are listed in Table 2, the bond lengths and
178 the thermal expansion values listed in Table 3, and the corresponding bond angles are listed in
179 Table 4. The underpinning structural rationale for this anisotropy in thermal expansion is
180 straightforward: the carbonate unit lies within the a - c plane, and the structural rigidity of this unit
181 likely limits the thermal expansion in both the a - and c -directions. In contrast, bonding within the
182 b -direction is predominantly associated with Na-O bonds, and to a lesser extent hydrogen
183 bonding (Figure 2).

184 Indeed, the carbonate group undergoes no resolvable changes in geometry over the
185 temperature range of this study, with no systematic changes in either bond length or bond angle.
186 It is slightly distorted from ideal three-fold symmetry: only the O₂-C₁-O₃ angle is close to 120°,
187 with the other two angles being near 116° and 124°. The carbonate group is also nearly planar,
188 with deviations from the plane being less than 0.005 Å.

189 The Na-O bonds in the structure all expand with increasing temperature (Figure 5), in
190 contrast to the prior results of Candlin (1956). The volume of the Na₁ octahedron increases
191 systematically with increasing temperature, and does not become more distorted with increasing
192 temperature, as measured by its quadratic elongation (Robinson et al. 1971). The Na₁-O₂ bonds
193 expand by 0.0188(18) Å while the Na₁-O₃ bonds expand by 0.0107(18) and 0.0103(18) Å over
194 the 240 K interval of these measurements. The volume of the Na₂ septahedron increases with
195 increasing temperature and becomes more elongated in the *b*-direction with an increase in
196 temperature. The longer of the two Na₂-O₁ bonds and the shorter of the two Na₂-O₄ bonds
197 expand substantially more than the other bonds in the septahedron, by 0.0322(19) Å and
198 0.0238(19) Å, respectively, while the other Na₂-O bonds of the septahedron expand by notably
199 smaller amounts (ranging from 0.0101(18) Å to 0.0232(16) Å).

200 The Na₂-O₁ bond and the Na₂-O₄ bond that are particularly responsive to temperature are
201 oriented in such a way that their expansion is directly associated with the enhanced thermal
202 expansion of the *b*-direction (Figure 6). The *b*-direction reflects the interplanar separation
203 between the carbonate units and between the hydrogens of the water molecules: this unit cell
204 parameter increases from 3.4583(5) to 3.4922(5) Å from 100 to 340 K. This ~1% linear
205 expansion in the separation between carbonate groups and water molecules in the *b*-direction
206 may represent an indication of the manner in which trona ultimately decomposes, with

207 progressively greater separations being accessed between water groups in the *b*-direction as
208 temperature is increased. The most parsimonious explanation for the means of water escape from
209 the structure during decomposition likely involves migration of the water molecules along the
210 structural channels between sodium polyhedra that are oriented along the *b*-axis of the structure.
211 It is likely that compaction of these channels produces the marked enhancement of the thermal
212 stability of trona that occurs under modest compression (Liu and Fleet 2009).

213 The refinements require that the H3 hydrogen atom remains disordered with 50%
214 occupancy between two O₂ sites at low temperatures, in accord with the 300 K structure derived
215 by Choi and Mighall (1982). Inclusion of the disordered H atom produced a substantial reduction
216 in the R-values of the final structure refinements. Thus, temperatures as low as 100 K are
217 insufficient to induce the structure to have discrete carbonate and bicarbonate units, in lieu of the
218 shared carbonate/bicarbonate character produced by the hydrogen disorder.

219 **High-pressure Raman and infrared spectral results and assignments**

220 Raman spectra of trona have been obtained on both compression and decompression;
221 representative Raman spectra are shown in Figure 7, and the change in frequency for each mode
222 as a function of pressure is plotted in Figure 8, with results tabulated in Table 5. The assignments
223 of the mid- (above ~500 cm⁻¹) and high-frequency Raman and infrared modes of trona have been
224 presented by Bertoluzza et al. (1981) and for the infrared bands by Novak et al. (1963), based on
225 comparisons with NaHCO₃-nahcolite, 3NaHCO₃Na₂CO₃-wegscheiderite, and deuterated samples
226 of these phases and trona (although Novak et al.'s (1963) assignments hinged on the hydrogen
227 being symmetric between carbonate groups, rather than disordered between two sites). The low-
228 frequency Raman vibrations of trona have not previously been assigned. However, based on (1)
229 their minimal shift in frequency with deuteration (Bertoluzza et al. 1981); (2) the ubiquity of

230 vibrations near 70, 90, 110 and 140 cm^{-1} in the sodium bicarbonate salts (Bertoluzza et al. 1981);
231 and (3) the presence of vibrations near the first three of these frequencies within the well-
232 understood Raman spectrum of NaOH (e.g., Kaneshaka et al. 1982), it appears that the assignment
233 of these vibrations to Na-O associated vibrations is robust. Which of these vibrations might be
234 Na-O stretching vibrations or Na-O-Na bending vibrations is less obvious: it is possible, by
235 analogy with NaOH, that the two lowest frequency of these bands are Na-O-Na bending
236 vibrations, with the vibrations between 140 and 180 cm^{-1} being associated with Na-O stretching
237 modes. This interpretation is in general accord with the smaller pressure shifts of the two lowest
238 frequency vibrations: compaction is likely to have less of an effect on interpolyhedral bending
239 vibrations.

240 Infrared spectra between ~ 550 and 1800 cm^{-1} on compression and decompression are
241 shown in Figure 9a,b, and the hydroxyl stretching vibrations are shown in Figure 10a,b, with
242 mode shifts shown in Figure 11a,b,c. The pressure dependences of the different infrared modes
243 provide insight into their assignments. In particular, the vibrations associated with the carbonate
244 group are readily identified through both their positions and pressure shifts. The infrared in-plane
245 bends (ν_4) of the carbonate group at 684 cm^{-1} and 710 cm^{-1} shift smoothly under compression
246 (Figure 12a). The corresponding Raman vibration at 699 cm^{-1} shifts at a rate intermediate
247 between those of the 684 and 710 cm^{-1} infrared bands. The infrared bands modestly increase in
248 their separation with pressure, implying that the distortion of the carbonate group (or of its local
249 environment) may weakly increase with pressure: site group-associated splitting likely produces
250 the separation of the two infrared bands (Greenaway et al. 1986). At ~ 5.7 GPa, an additional
251 infrared mode for which the pressure shift is compatible with the other in-plane bends becomes

252 resolvable near 670 cm^{-1} : this band may simply be separating from a highly-absorbing broad
253 feature near 550 cm^{-1} .

254 The IR active mode at 805 cm^{-1} shifts rapidly with increasing pressure and crosses
255 through, but does not appear to resonantly interact with, the carbonate out-of-plane bend (ν_2) at
256 850 cm^{-1} (Figure 11a). The former band has been attributed to an H_2O -associated vibration,
257 based on its non-appearance in deuterated spectra (Novak et al., 1963): the most likely
258 assignment, based on its frequency, is to an H_2O -libration (e.g., Lutz, 1988), and its robust
259 pressure shift is in accord with increasing hydrogen-bonding of the water-molecule under
260 pressure. An alternate possibility, discussed below, is that it could be associated with vibrational
261 transitions associated with the double-well potential of the disordered hydrogen of the hydroxyl
262 unit. The out-of-plane bend at 850 cm^{-1} shifts by $-1.0\text{ cm}^{-1}/\text{GPa}$ with increasing pressure: this
263 negative shift is in accord with the behavior of this vibration in a wide suite of other carbonates,
264 and is likely generated by increases in cation-oxygen bond strength under pressure (e.g., Kraft et
265 al. 1991; Williams et al. 1992; Gillet et al. 1993; Catalli et al. 2005). The asymmetric stretch (ν_3)
266 of the carbonate unit falls at 1461 cm^{-1} , and evolves a high-frequency shoulder that becomes
267 deconvolvable above $\sim 4\text{ GPa}$: these bands have almost identical pressure shifts.

268 For the bands between 1550 and 1800 cm^{-1} , our assignments differ from those of Novak
269 et al. (1963) and Bertoluzza et al. (1981). In particular, the band with a zero pressure frequency
270 of 1557 cm^{-1} has a pressure shift that is markedly larger than any other within trona: nearly 12
271 $\text{cm}^{-1}/\text{GPa}$. Both the location and pressure shift of this band indicate that it is the first overtone of
272 the vibration at 806 cm^{-1} , shifted to lower frequency by anharmonicity. Furthermore, its behavior
273 strongly suggests that its intensity is enhanced by a resonant interaction with the band at 1749
274 cm^{-1} : at low pressures, its intensity renders it barely resolvable, but it increases in strength as it

275 approaches the higher frequency peak (Figure 9a). Hence, the symmetry of this overtone is likely
276 the same as that of the band at 1749 cm^{-1} , and the two undergo increased levels of Fermi
277 resonance with one another as pressure is increased. The coupling constant (which is equal to
278 half the closest approach of these bands) of these modes within trona appears to be on the order
279 of 50 cm^{-1} , or a bit over half an order of magnitude larger than previously observed resonant
280 couplings between vibrations in hydrous phases (e.g., Duffy et al. 1995; Knittle et al. 2001). As
281 with prior studies (Novak et al. 1963; Bertoluzza et al. 1981), we do not resolve an unambiguous
282 H-O-H bending vibration in our spectra: given the somewhat broadened (relative to free H_2O) H-
283 O-H angle in trona of 107.4° (Choi and Mighell 1982), such a vibration would be anticipated to
284 occur near 1600 cm^{-1} (e.g., Lutz 1988). Unless the band at 1698 cm^{-1} is the H-O-H stretch, which
285 is unlikely, as this is an anomalously high frequency for such a vibration (particularly given the
286 wide H-O-H angle in this phase: e.g., Lutz 1988), it appears that this vibration is not
287 characterized.

288 The origins of the infrared bands at 1698 and 1749 cm^{-1} are thus problematic: the former
289 band was attributed by Novak et al. (1963) and Bertoluzza et al. (1981) to either a high-lying
290 asymmetric stretch of the carbonate unit, or a water-associated vibration. The latter interpretation
291 is consistent with the shift of these bands on deuteration: the frequency ratio between the
292 hydrogen-bearing vibrations and the deuterium-bearing vibrations is near 1.09 (Novak et al.
293 1963; Bertoluzza et al. 1981). Within crystalline carbonates, it has long been appreciated that
294 overtones and combinations commonly fall in this spectral range as well (Ross and Goldsmith
295 1964): such combinations can be the $2 \times \nu_2$ (e.g., Kraft et al. 1991) or $\nu_1 + \nu_4$ vibrations of the
296 carbonate group (e.g., Catalli et al. 2005), and can often be distinguished by their pressure shifts.
297 However, neither of the bands' pressure shifts appears compatible with an obvious combination

298 band. The possibility that these bands might be associated with C=O vibrations, which occur in
299 KHCO_3 at frequencies as high as 1650 cm^{-1} (e.g., Dopieralski et al. 2010) does not explain their
300 shift on deuteration. With respect to these vibrations, it is worth noting that the disordered
301 hydrogen positions of the hydroxyl unit in trona occupy a symmetric, double-well potential that
302 is almost linearly oriented between the O(2) oxygens within the structure. As noted for trona
303 (among other phases) by Sokolov et al. (1988, 1990), a quantum mechanical analysis of this
304 configuration gives rise to a number of energy levels associated with the protons, and optical
305 transitions between these levels (e.g., Romanowski and Sobczyk 1977). In short, multiple optical
306 transitions can be generated between different proton states, including the ground and excited
307 states. Given the approximate nature of the theory, it is possible that either the 1698 or 1740 cm^{-1}
308 bands could be generated by a transition between either the fundamental and a higher-lying
309 excited state, or between excited states of the proton (which would imply a marked temperature
310 dependence for the absorption). If this were the case, the ground state to first excited state
311 transition in trona would be anticipated to occur at substantially lower frequencies, and could be
312 associated with the 800 cm^{-1} band: this might provide a natural explanation for the strong Fermi
313 resonant coupling constant between the overtone of this transition and the transition between the
314 two excited states. Indeed, Fillaux (1983) proposed that a highly temperature-dependent infrared
315 band near 1870 cm^{-1} in KHCO_3 may be associated with transitions between excited states of the
316 hydroxyl stretching vibration within a double minimum potential. An appealing aspect of this
317 explanation is that compaction of the O-O distance generally produces increases in the
318 frequencies of transitions associated with excited states (Romanowski and Sobczyk 1977;
319 Sokolov et al. 1988, 1990), and thus a positive pressure shift of these vibrations would be
320 anticipated, in accord with our observations.

321 Above 3000 cm^{-1} , we fit three separate peaks to the infrared spectra, with zero pressure
322 frequencies of 3050, 3449 and 3530 cm^{-1} : the locations of the first and third of these are in
323 reasonable agreement with Novak et al. (1963) and Bertoluzza et al. (1981), while the
324 intermediate peak is required to adequately match the shape of the observed hydroxyl stretching
325 envelope. The initial pressure shift of these peaks is generally similar, with each shifting to lower
326 frequencies on compression, implying that hydrogen bonding increases with pressure within
327 trona. The assignment of these peaks to hydroxyl stretching vibrations associated with the water
328 molecule is compatible with the hydrogen bonding lengths of water within trona, based on
329 general correlations between band frequency and O-O separation (e.g., Nakamoto et al. 1955).

330 **High-Pressure Phase Transitions**

331 The low frequency Raman vibrations with ambient pressure frequencies at ~ 71 and 100
332 cm^{-1} are associated with vibrations of the Na-O polyhedra: they shift non-linearly to higher
333 frequency under compression. At ~ 7.0 GPa, the lower frequency band splits, and its lower
334 frequency component and the continuation of the 100 cm^{-1} band each abruptly begin to shift to
335 lower frequency. This negative shift persists until ~ 14.5 GPa (Figure 8a). Other Raman peaks
336 may undergo modest shifts in their pressure-dependence at this pressure (particularly the 139
337 and 155 cm^{-1} bands), but no discontinuities in peak positions are observed. The combination of
338 mode splitting and shifts in pressure-dependences suggests that the phase transition near ~ 7.0
339 GPa is second order in character and, based on its Raman spectral signature, predominantly
340 involves changes in the geometry of the sodium polyhedra.

341 The infrared spectra are compatible with this interpretation of the ~ 7.0 GPa transition:
342 specifically, the pressure dependence of the in-plane bending vibration with a zero-pressure
343 frequency of 710 cm^{-1} shifts, and changes in the H_2O rotational vibration and its overtone at 805

344 and 1557 cm^{-1} , respectively, occur. A shift in sign of the pressure dependence of the O-H
345 stretching vibrations with zero pressure frequencies of 3449 cm^{-1} and 3530 cm^{-1} also occurs at
346 this pressure, indicating that a shift in the hydrogen bonding geometry has occurred associated
347 with this transition. Each of these vibrations involves oxygen anions that form part of the sodium
348 septahedron, and hence this transition is plausibly produced by a shift in the geometry of this
349 sodium polyhedral unit.

350 At $\sim 14.5\text{ GPa}$, changes in mode frequencies, the appearance of new bands, and
351 disappearance of bands imply that a second phase transition takes place. In particular, a change
352 in the nature of the lowest frequency Raman vibrational modes at $\sim 14.5\text{ GPa}$ suggests that the
353 coordination geometry of the Na-O polyhedra changes significantly (Figure 8a): a new band
354 appears near 85 cm^{-1} , the band with a zero-pressure frequency near 155 cm^{-1} disappears, and the
355 frequency of the mode with a zero pressure frequency near 172 cm^{-1} drops in frequency by ~ 10
356 cm^{-1} . At higher frequencies, the in-plane bend, the symmetrical stretch, and the asymmetric
357 stretches of the carbonate group each shift discontinuously to lower frequency at this pressure
358 (Figures 8b, 11b), and continue to shift to higher frequency with increases in pressure. The
359 symmetrical stretch peak of the carbonate group becomes asymmetrical at $\sim 11.0\text{ GPa}$ and splits
360 at $\sim 14.5\text{ GPa}$ and remains split up to 25.4 GPa . The pressure dependence of the H_2O vibrational
361 mode at 3049 cm^{-1} changes sign at this transition (and a weak positive discontinuity in mode
362 frequency may be present), and begins to shift positively at pressures greater than 14.5 GPa
363 (Figure 11c). It is near this pressure that a new hydroxyl stretching band appears at $\sim 3580\text{ cm}^{-1}$:
364 this band ultimately becomes the dominant feature in the hydroxyl region of the spectrum
365 (Figure 10a, 11c). The band with a zero pressure frequency near 1750 cm^{-1} that we have
366 attributed to transitions associated with the O-H \cdots O strongly bound hydroxyl unit disappears at

367 this transition, which may imply that the double-welled potential (and associated H-disorder) is
368 not present within this phase.

369 In terms of its effect on the carbonate group vibrations (a decrease in the frequencies, and
370 hence force constants, of the carbonate group), the manifestations of this higher pressure
371 transition closely resemble those of a transition in KHCO_3 that occurs near 2.8 GPa (Kagi et al.
372 2003): a transition associated with tilting of the carbonate units, displacement of molecular layers
373 relative to one another, and an increase in K-coordination from 8- to 10-fold (Allan et al. 2007).
374 Additionally, a splitting of the symmetric stretching vibration of the carbonate group occurs at
375 this transition, indicating that either multiple carbonate group environments may be present in
376 the high-pressure phase, or that the unit cell may be expanded. The weakening of the carbonate
377 bonds may be associated with a displacement in the three-membered sodium polyhedral units
378 (e.g., Figure 2) relative to one another, with accompanying elongation of the C-O bonds within
379 the carbonate units. This transition also appears to be associated with a notable decrease in
380 hydrogen bonding, as manifested by the positive pressure shifts of the hydroxyl stretching bands
381 and the appearance of a new, higher frequency hydroxyl stretching band. This is again
382 compatible with a shift in the neighboring sodium polyhedral units relative to one another. It is
383 also possible that, due to the large number of water molecules present within trona and their
384 closely juxtaposed positions, hydrogen-hydrogen repulsion may become increasingly important
385 within the phase of trona that occurs above 14.5 GPa.

386 This transition is reversible, but with substantial hysteresis: for example, the symmetric
387 stretch of the carbonate group remains split during decompression down to ~ 2.5 GPa (Figure 8b).
388 Both the carbonate in-plane bend and symmetric stretch return to within a few wavenumbers of
389 their initial peak locations. The low frequency vibrations (Figure 8a) show similar shifts upon

390 decompression and also return to within a few wavenumbers of their initial peak locations. Thus,
391 the higher pressure transition we observe is, based on the observed hysteresis, likely first-order in
392 character: however, the high-pressure phase cannot be quenched to ambient pressures at 300 K.

393 **Novel Resonance Effects**

394 An interesting feature of the infrared spectrum of trona (Figure 1) is the transmission
395 window that is present at 1050 cm^{-1} . This sharp decrease in absorbance was first noted in trona
396 by Novak et al. (1963), and assigned to a peculiar resonance effect first observed by Evans and
397 Wright (1960) in the infrared spectrum of *m*-toluidine. This effect has been further studied, and
398 quantitatively modeled, by Evans (1960, 1962) and Claydon and Sheppard (1969). Trona may be
399 the single example observed to date of this “Evans window” effect in minerals: in short, a
400 transmission maximum is generated when a broad band overlaps a sharp fundamental band of the
401 same symmetry. A form of Fermi resonance thus occurs, with the intensity of the fundamental
402 band being resonantly redistributed at frequencies surrounding the fundamental, and a
403 transmission window within the broad band being produced at the frequency of the sharp
404 fundamental (Evans and Wright 1960). In the case of trona, the transmission window is the result
405 of the symmetrical carbonate stretch interacting with a broad band at a similar frequency. The
406 nature of the broad band is unclear: it appears that it is a combination band or overtone
407 associated with a hydroxyl or water vibration (presumably a libration or translation), as the
408 transmission maximum disappears within deuterated samples (Novak et al., 1963).

409 We are able to monitor the pressure shift of this transmission window under compression
410 and decompression (Figure 12a,b). The transmission window shifts smoothly with increasing
411 pressure into a diamond absorption region and returns upon decompression (Figure 12a). Its
412 pressure shift is in close accord with the shift of the corresponding Raman (ν_1) symmetric

413 stretching vibration, confirming the identification of this spectral hole as being associated with
414 this sharp fundamental vibration.

415 **Mode Grüneisen Parameters**

416 Using the pressure derivative of a vibrational frequency ν_i for a mode i , ($d\nu_i/dP$), a mode
417 Grüneisen parameter (γ_i) can be calculated using $\gamma_i = K_0/\nu_{0i} (d\nu_i/dP)$. Here, K_0 is the bulk modulus
418 of trona, which was estimated to be 36 GPa, as calculated from the P- and S- wave velocities in
419 trona-dominated strata and the known density of trona (Ge et al. 2012). This value is of unknown
420 accuracy. However, it lies in the vicinity of that of other water-rich evaporite minerals (for
421 example, the bulk modulus of gypsum is ~45 GPa: Stretton et al. 1997). The ν_{0i} values were
422 determined by infrared and Raman spectroscopy at room temperature and pressure, and the
423 calculated $d\nu_i/dP$ and γ_i are listed in Table 5. For comparison, the thermodynamic value of the
424 Grüneisen parameter can be determined using our thermal expansion (α), coupled with the bulk
425 modulus of 36 GPa (K_0), the density (ρ), and the heat capacity at 300 K (C_p) from Haynes (2003)
426 using $\gamma_i = \alpha K_0/\rho C_p$. The calculated thermodynamic Grüneisen parameter is 1.06: our overall
427 average mode Grüneisen parameter for the fundamental bands in Table 5 is 0.48. This
428 discrepancy is certainly associated with the oversampling of high-frequency, low-Grüneisen
429 parameter molecular modes in our study, and in particular in our mid-infrared spectral
430 measurements. An averaging of our Raman modes, which sample both low- and high-frequency
431 portions of the trona spectrum, yield an average value of 0.91, which is in substantially closer
432 accord with the thermodynamic value. Unsurprisingly, the dominant contributors to the
433 thermodynamic Grüneisen parameter are low-frequency modes, and particularly modes that are
434 likely to be associated with the Na-O polyhedra.

435 **Implications**

436 The behavior of trona under extreme conditions is useful for understanding late-stage
437 peralkaline magmatic processes (e.g., Markl and Baumgartner 2002), as well as the behavior of
438 water molecules within a carbonate-dominated framework. Notably, the interactions between
439 water/hydrogen and carbonate units are quite insensitive to pressure: while hydrogen bonding
440 weakly increases with compression in trona (and may decrease across high-pressure polymorphic
441 transitions), the carbonate unit behaves in a similar manner to the carbonate unit in other
442 carbonate minerals under high pressure such as aragonite and dolomite (Kraft et al. 1991; Gillet
443 et al. 1993), siderite and rhodochrosite (Santillan and Williams 2004), and witherite (Lin and Liu
444 1997). Hence, at least within trona, carbonate ions and water molecules behave as largely
445 independent molecular units, with limited interactions, under compression.

446 As an industrial material whose thermal stability is important in its usage as both a
447 sorbent and scrubber of SO₂ (Kong and Wood 2010; Su et al. 2011; Sutcu and Eker 2013) and
448 CO₂ (Ficicilar and Dogu, 2006), the effect of temperature appears to be most notably manifested
449 in the sodium septahedron within the structure. The thermal expansions of two bonds in this
450 polyhedron appear to be anomalous (as is the thermal expansion of the *b*-axis), and this
451 expansion may be a key contributor to the thermal stability limit of trona. In this respect, it is
452 notable that substitution of potassium into trona induces both a change in crystal symmetry and a
453 weak increase in thermal stability from ~330 K (Cho et al. 2008) to 341 K (Adam and Cirpus
454 1996). Hence, enhancing the thermal stability of trona may require substitution into the
455 septahedral site: a site that is not amenable to substitution by heavier elements (Adam and Cirpus
456 1996). Finally, we note that the disordered hydrogen position within trona could be associated
457 with tunneling and quantum correlation effects: these are hinted at by our possible assignment of
458 bands between 1690 and 1750 cm⁻¹ to transitions between the ground and excited states of the O-

459 H⁺O unit. Such anomalous quantum effects in phases containing protons with multiple sites
460 have been extensively documented within KHCO₃ (Fillaux et al. 2006; Fillaux 2007), and the
461 disordered hydrogens associated with the O-H⁺O units within trona may represent candidates for
462 similar quantum effects.

463 **Acknowledgements**

464 The authors would like to thank the organizers of the American Crystallographic
465 Association summer course in chemical crystallography: Dr. Amy Sarjeant, Ms. Charlotte Stern,
466 and Dr. Allen Oliver. The authors would also like to thank Dr. Simon Teat at the ALS for
467 assistance, Dr. Paul Mattern at UCSC for assistance, and three anonymous reviewers for
468 constructive comments. Work partially supported by NSF through EAR-1215745, and
469 COMPRES under NSF Cooperative Agreement EAR 11-57758. The Advanced Light Source is
470 supported by the Director, Office of Science, Office of Basic Energy Sciences, of the U.S.
471 Department of Energy under Contract No. DE-AC02-05CH11231.

472

473 **References**

- 474 Adam, A., and Cirpus, V. (1996) Darstellung und Struktur der ersten gemischten
475 Alkalimetallhydrogencarbonate NaA₂[H(CO₃)₂]·2H₂O mit A = K, Rb. *Zeitschrift für*
476 *Anorganische Allgemeine Chemie*, 622, 2023-2030.
- 477 Allan, D.R., Marshall, W.G., and Pulham, C.R. (2007) The high-pressure crystal structure of
478 potassium hydrogen carbonate (KHCO₃). *American Mineralogist*, 92, 1018-1025.
- 479 Arakcheeva, A., Bindi, L., Pattison, P., Meisser, N., Chapuis, G., and Pekov, I. (2010) The
480 incommensurately modulated structures of natural natrite at 120 and 293 K from
481 synchrotron X-ray data, *American Mineralogist*, 95, 574-581.

- 482 Bacon, G.E., and Curry, N.A. (1956) A neutron-diffraction study of sodium sesquicarbonate.
483 *Acta Crystallographica*, 9, 82-85.
- 484 Ballirano, P., and Melis, E. (2009) Thermal behaviour and kinetics of dehydration of gypsum in
485 air from in situ real-time laboratory parallel beam X-ray powder diffraction. *Physics and*
486 *Chemistry of Minerals*, 36, 391-402.
- 487 Bertoluzza, A., Monti, P., Morelli, M.A., and Battaglia, M.A. (1981) A Raman and infrared
488 spectroscopic study of compounds characterized by strong hydrogen bonds. *Journal of*
489 *Molecular Structure*, 73, 19-29.
- 490 Brand, H.E.Q., Fortes, A.D., Wood, I.G., Knight, K.S., and Vocadlo, L. (2009) The thermal
491 expansion and crystal structure of mirabilite (Na₂SO₄·10H₂O) from 4.2 to 300 K as
492 determined by time-of-flight neutron powder diffraction. *Physics and Chemistry of*
493 *Minerals*, 36, 29-46.
- 494 Brown, C.J., Peiser, H.S., and Turner-Jones, A. (1949) The crystal structure of sodium
495 sequicarbonate. *Acta Crystallographica*, 2, 167-174.
- 496 Brusentsova, T.N., Peale, R.E., Maukonen, D., Harlow, G.E., Boesenberg, J.S., and Ebel, D.
497 (2010) Far infrared spectroscopy of carbonate minerals. *American Mineralogist*, 95,
498 1515-1522.
- 499 Candlin, R. (1956) Thermal changes in the structure of sodium sequicarbonate. *Acta*
500 *Crystallographica*, 9, 545-554.
- 501 Catalli, K., Santillan, J., and Williams, Q. (2005) A high pressure infrared spectroscopic study of
502 PbCO₃-cerussite: Constraints on the structure of the post-aragonite phase. *Physics and*
503 *Chemistry of Minerals*, 32, 412-417.

- 504 Catalli, K., and Williams, Q. (2005) A high-pressure phase transition of calcite-III. *American*
505 *Mineralogist*, 90, 1679-1682.
- 506 Cho, K.J., Keener, T.C., and Khang, S.-J. (2008) A study on the conversion of trona to sodium
507 bicarbonate, *Powder Technology*, 184, 58-63.
- 508 Choi C.S., and Mighell A.D., (1982) Neutron diffraction study of sodium sesquicarbonate
509 dihydrate. *Acta Crystallographica*, B38, 2874-2876.
- 510 Claydon, M.F., and Sheppard, N. (1969) The nature of “A, B, C”-type infrared spectra of
511 strongly hydrogen-bonded systems; pseudo-maxima in vibrational spectra. *Journal of the*
512 *Chemical Society D: Chemical Communications*, 23, 1431-1433.
- 513 Dolomanov O.V., Bourhis L.J., Gildea R.J., Howard J.A.K., and Puschmann, H. (2009) OLEX2:
514 a complete structure solution, refinement and analysis program.
515 *J. Appl. Cryst.* 42, 339-341.
- 516 Dopieralski, P.D., Latajka, Z., and Olovsson, I. (2010) Proton-transfer dynamics in the $(\text{HCO}_3^-)_2$
517 dimer of KHCO_3 from Car-Parrinello and path-integrals molecular dynamics calculations.
518 *Acta Crystallographica*, B66, 222-228.
- 519 Duffy, T.S., Meade, C., Fei, Y., Mao, H.K., and Hemley, R.J. (1995) High-pressure phase
520 transition in brucite, $\text{Mg}(\text{OH})_2$. *American Mineralogist*, 80, 222-230.
- 521 Ekosse, G.I.E. (2010) X-ray diffraction study of kanwa used as active ingredient in achu soup in
522 Cameroon. *African Journal of Biotechnology*, 9, 7928-7929.
- 523 Evans, J.C. (1960) Further studies of unusual effects in the infrared spectra of certain molecules.
524 *Spectrochimica Acta*, 16, 994-1000.
- 525 Evans, J.C. (1962) Narrow transmission regions within broad infrared absorption bands in solids.
526 *Spectrochimica Acta*, 19, 507-512.

- 527 Evans, J.C., and Wright, N. (1960) A peculiar effect in the infrared spectra of certain molecules.
528 *Spectrochimica Acta*, 16, 352-357.
- 529 Ficicilar, B., and Dogu, T. (2006) Breakthrough analysis for CO₂ removal by activated
530 hydrotalcite and soda ash. *Catalysis Today*, 115, 274-278.
- 531 Figg, J., Moore, A.E., and Gutteridge, W.A. (1976) On the occurrence of the mineral trona
532 (Na₂CO₃ NaHCO₃ 2H₂O) in concrete deterioration products. *Cement and Concrete*
533 *Research*, 6, 691-696.
- 534 Fillaux, F. (1983) Calculations of infrared and Raman band profiles of strong hydrogen bonds.
535 OH stretching bands and proton dynamics in crystalline potassium hydrogen carbonate.
536 *Chemical Physics*, 74, 405-412.
- 537 Fillaux, F. (2007) Proton transfer in the KHCO₃ and benzoic acid crystals: A quantum view.
538 *Journal of Molecular Structure*, 844/845, 308-318.
- 539 Fillaux, F., Cousson, A., and Gutmann, M.J. (2006) Macroscopic quantum entanglement and
540 'super-rigidity' of protons in the KHCO₃ crystal from 30 to 300 K. *Journal of Physics:*
541 *Condensed Matter*, 18, 3229-3249.
- 542 Ge, M., Wang, H., Schissler, A., and Ramani, R. (2012). Measuring pillar width in trona mines
543 using a body wave based in-seam seismic technique. *International Journal of Rock*
544 *Mechanics and Mining Sciences*, 53, 10-17.
- 545 Gillet, P., Biellmann, C., Reynard, B., and McMillan, P. (1993) Raman spectroscopic studies of
546 carbonates: Part 1. High-pressure and high-temperature behavior of calcite, magnesite,
547 dolomite and aragonite. *Physics and Chemistry of Minerals*, 20, 1-18.

- 548 Greenaway, A.M., Dasgupta, T.P., Koshy, K.C., and Sadler G.G. (1986) A correlation between
549 infrared stretching mode absorptions and structural angular distortions for the carbonato
550 ligand in a wide variety of complexes. *Spectrochimica Acta A*, 42, 949-954.
- 551 Haynes, H.W. (2003) Thermodynamic solution model for trona brines. *AIChE Journal*, 49, 1883-
552 1894.
- 553 Kanesaka, I., Tsuchida, M., and Kawai, K. (1982) Vibrational spectra and normal coordinate
554 analysis of NaOX (X = H or D). *Journal of Raman Spectroscopy*, 13, 253-256.
- 555 Knittle, E., Phillips, W., and Williams, Q. (2001) An infrared and Raman spectroscopic study of
556 gypsum at high pressures. *Physics and Chemistry of Minerals*, 28, 630-640.
- 557 Kong Y., and Wood M.D. (2010) Dry injection of trona for SO₃ control. *Power*, 154, 114-118.
- 558 Kraft, S., Knittle, E., and Williams, Q. (1991). Carbonate stability in the Earth's mantle: a
559 vibrational spectroscopic study of aragonite and dolomite at high pressures and
560 temperatures. *Journal of Geophysical Research: Solid Earth*, 96, 17997-18009.
- 561 Lennie, A.R., Tang, C.C., and Thompson, A.P. (2004) The structure and thermal expansion
562 behavior of ikaite, CaCO₃·6H₂O, from T = 114 to T = 293 K. *Mineralogical Magazine*,
563 68, 135-146.
- 564 Lin, C.C., and Liu, L.G. (1997) High-pressure Raman spectroscopic study of post-aragonite
565 phase transition in witherite (BaCO₃). *European Journal of Mineralogy*, 9, 785-792.
- 566 Liu, X., and Fleet, M.E. (2009) Phase relations of nahcolite and trona at high PT conditions.
567 *Journal of Mineralogical and Petrological Sciences*, 104, 25-36.
- 568 Lutz, H.D. (1988) Bonding and structure of water molecules in solid hydrates. Correlation of
569 spectroscopic and structural data. *Structure and Bonding*, 69, 97-125.

- 570 Markgraf, S.A., and Reeder, R.J. (1985) High-temperature structure refinements of calcite and
571 magnesite. *American Mineralogist*, 70, 590-600.
- 572 Mao, H.K., Xu, J.A., and Bell, P.M. (1986) Calibration of the ruby pressure gauge to 800 kbar
573 under quasi-hydrostatic conditions. *Journal of Geophysical Research*, 91, 4673-4676.
- 574 Markl, G., and Baumgartner, L. (2002) pH changes in peralkaline late-magmatic fluids.
575 *Contributions to Mineralogy and Petrology*, 144, 331-346.
- 576 Nakamoto, K., Margoshes, M., and Rundle, R.E. (1955) Stretching frequencies as a function of
577 distances in hydrogen bonds. *Journal of the American Chemical Society*, 77, 6480-6486.
- 578 Nielsen, J.M. (1999) East African magadi (trona): Fluoride concentration and mineralogical
579 concentration. *Journal of African Earth Sciences*, 29, 423-428.
- 580 Novak, A., Saumagne, P., and Bok, L.D.C. (1963) Etude par spectroscopie infrarouge de
581 quelques hydrogenocarbonates alcalins: NaHCO_3 , NH_4HCO_3 , KHCO_3 , et du
582 sesquicarbonate de sodium $\text{Na}_2\text{CO}_3\cdot\text{NaHCO}_3\cdot 2\text{H}_2\text{O}$. *Journal de Chimie Physique*, 60,
583 1385-1395.
- 584 Pertlik, F. (1986) Ein vergleich von ergebnissen routine assiger strukturbestimmungen mittels
585 rontgen- BZW. Neutronen-einkristalldaten am beispiel der trona, $\text{Na}_3\text{H}[\text{CO}_3]_2\cdot 2\text{H}_2\text{O}$.
586 *Mitteilungen Osterreichischen Mineralogischen Gesellschaft*, 131, 7-14.
- 587 Robinson, K., Gibbs, G.V., and Ribbe, P.H., (1971) Quadratic elongation: A quantitative
588 measure of distortion in coordination polyhedra. *Science*, 172, 567-570.
- 589 Romanowski, H., and Sobczyk, L. (1977) A stochastic approach to the IR spectra of the OHO
590 symmetrical hydrogen bond. *Chemical Physics*, 19, 361-370.

- 591 Ross, S.D., and Goldsmith, J. (1964) Factors affecting the infrared spectra of planar anions with
592 D_{3h} symmetry-I. Carbonates of the main group and first row transition elements.
593 *Spectrochimica Acta*, 20, 781-784.
- 594 Santillan, J., and Williams, Q. (2004) A high-pressure infrared and X-ray study of $FeCO_3$ and
595 $MnCO_3$: comparison with $CaMg(CO_3)_2$ -dolomite. *Physics of the Earth and Planetary*
596 *Interiors*, 143, 291-304.
- 597 Sheldrick G.M. (2008) A short history of *SHELX*. *Acta Cryst.* A64, 112-122.
- 598 Sokolov, N.D., Vener, M.V., and Savel'ev, V.A. (1988) Tentative study of strong hydrogen bond
599 dynamics. Part I. Geometric isotope effects. *Journal of Molecular Structure*, 177, 93-110.
- 600 Sokolov, N.D., Vener, M.V., and Savel'ev, V.A. (1990) Tentative study of strong hydrogen bond
601 dynamics. Part II. Vibrational frequency considerations. *Journal of Molecular Structure*,
602 222, 365-386.
- 603 Stretton, I.C., Schofield, P.F., Hull, S., and Knight, K.S. (1997) The static compressibility of
604 gypsum. *Geophysical Research Letters*, 24, 1267-1270.
- 605 Sutcu H., and Eker Y. (2013) The removal of sulfur from Dursunbey and Iskilip lignites in
606 Turkey, using natural trona: 1. The effect of the thermal method. *Energy Sources Part A-*
607 *Recovery Utilization and Environmental Effects*, 35, 83-91.
- 608 Williams, Q., Collerson, B., and Knittle, E. (1992) Vibrational spectra of magnesite and calcite-
609 III at high-pressures. *American Mineralogist*, 77, 1158-1165.
- 610 Yoo M., Han S.J., and Wee J.H. (2013) Carbon dioxide capture capacity of sodium hydroxide
611 aqueous solution, *Journal of Environmental Management*, 114, 512-519.
- 612
613

- 614
615 Figure 1. Representative ambient temperature and pressure infrared and Raman spectra of trona.
616
617 Figure 2. Crystal structure of trona at 300K looking down the b-axis note: the dynamically
618 disordered H₃ atom is represented with light hatchmarked circles (H-atom positions from Choi
619 and Mighell 1982). Unit cell is outlined in the solid gray line. Image generated using
620 CrystalMaker ® v8.7.6.
621
622 Figure 3. Unit cell volume of trona as a function of temperature.
623
624 Figure 4. Normalized unit-cell parameters as a function of temperature, with lines representing
625 least square fits to our observations. With temperature, the *b*-axis changes by almost a factor of
626 three greater than the *a* and *c* axes.
627
628 Fig 5. Normalized Na-O bond lengths as a function of temperature, with lines representing least
629 square fits to our observations. All Na-O bonds expand with increasing temperature. The long
630 Na₂-O₁ and the short Na₂-O₄ bonds expand substantially more than the any other Na-O bond
631 with temperature.
632
633 Figure 6. Na octahedral and septahedral sites, with changes in Na-O bond angles, and distances
634 between Na₁-Na₁, Na₂-Na₂, O₁-O₁, O₃-O₃, and O₁-O₄ bonds from 100 K to 340 K being labeled.
635 Crystal structure image generated using CrystalMaker ® v8.7.6.
636
637 Figure 7. Representative Raman spectra of trona up to 25.4 GPa (a) low frequency under
638 compression (b) carbonate ν₁ peak under compression (c) low frequency under decompression
639 (d) carbonate ν₁ under decompression. Because multiple runs were conducted with trona crystals
640 mounted in different orientations, peak intensities vary between spectra (this is particularly
641 notable in the contrast between the low frequency spectra of samples at 2.0 and 3.9 GPa).
642
643 Figure 8. Peak positions of observed Raman modes in trona as a function of pressure at room
644 temperature, solid circles are compression open circles are decompression. Error bars are smaller
645 than symbols, and vertical dashed lines indicate likely phase transitions. (a) low frequency (b)
646 carbonate asymmetric stretch and I-P bend.
647
648 Figure 9 Representative infrared spectra of trona in the mid-infrared region up to 24.2 GPa (a)
649 under compression (b) under decompression.
650
651 Figure 10 Representative infrared spectra of trona in the hydroxyl stretching region up to 24.2
652 GPa (a) under compression (b) under decompression.
653
654 Figure 11. Peak positions of observed infrared modes in trona as a function of pressure at room
655 temperature. Solid circles are on compression, and open circles are on decompression. Error bars
656 are smaller than the symbols, and vertical dashed lines indicate likely phase transitions. (a)
657 carbonate bending vibrations, H₂O libration, and transmission window; (b) carbonate asymmetric
658 stretches, 1st overtone of 806 cm⁻¹, and a transition or combination band; and (c) O-H stretches of
659 the H₂O molecule.

660
661 Figure 12. Infrared spectra of the transmission window shifting as a function of pressure (a)
662 under compression (b) under decompression. Inset in 12b: Schematic diagram of Fermi
663 resonance effect, with the dashed line showing two overlapping modes (one sharp, and one
664 broad) in the absence of a Fermi resonance, and the solid line illustrating the resultant spectrum
665 when Fermi resonance occurs (after Claydon and Sheppard, 1969).
666
667
668
669
670
671
672
673
674
675
676
677
678
679
680
681
682
683
684
685
686
687
688
689
690
691
692
693
694
695
696
697
698
699
700
701
702
703
704
705

706

707

708

709

710

Table 1: Unit cell parameters and experimental details of trona single-crystal refinements.

T (± 2) (K)	100	200	300	320	330	340
Wavelength (\AA)	1.54187 (1)	1.54187 (1)	1.54187 (1)	0.61990 (1)	0.61990 (1)	0.61990 (1)
a (\AA)	20.366 (3)	20.370 (4)	20.4124 (10)	20.398 (3)	20.402 (4)	20.400 (3)
b (\AA)	3.4583 (5)	3.4749 (7)	3.4927 (2)	3.4887 (5)	3.4881 (6)	3.4922 (5)
c (\AA)	10.2946 (13)	10.3146 (19)	10.3327 (4)	10.3248 (16)	10.3085 (18)	10.3279 (14)
β ($^\circ$)	106.483 (9)	106.484 (14)	106.471 (3)	106.545 (8)	106.552 (10)	106.469 (7)
Volume (\AA^3)	695.26 (17)	700.1 (2)	706.43 (6)	704.33 (19)	703.20 (2)	705.59 (8)
Z	4	4	4	4	4	4
N _{reflections}	624	621	625	1615	1613	1623
N _{unique}	582	560	550	1509	1466	1425
R1 (%)	3.41	4.08	4.26	4.97	4.97	4.18
wR2 (%)	10.65	10.92	11.09	13.88	14.01	13.06
GooF	1.646	1.081	1.112	1.164	1.119	1.167

711

712

713 Table 2: Fractional atomic coordinates as a function of temperature (refined anisotropically).
 714

Atom	T (K)	x	y	z
Na ₁	100	0.0000	0.7475 (3)	0.2500
	200	0.0000	0.7466 (3)	0.2500
	300	0.0000	0.7462 (3)	0.2500
	320	0.0000	0.7461 (2)	0.2500
	330	0.0000	0.7460 (2)	0.2500
	340	0.0000	0.7461 (2)	0.2500
Na ₂	100	0.15092 (4)	0.1598 (2)	0.42574 (7)
	200	0.15081 (5)	0.1620 (3)	0.42569 (9)
	300	0.15064 (5)	0.1641 (3)	0.42549 (8)
	320	0.15053 (3)	0.16492 (17)	0.42604 (6)
	330	0.15050 (4)	0.16531 (19)	0.42606 (6)
	340	0.15053 (3)	0.1657 (16)	0.42604 (6)
C ₁	100	0.09308 (10)	0.2662 (5)	0.10314 (19)
	200	0.09316 (12)	0.2648 (6)	0.1033 (2)
	300	0.09337 (11)	0.2638 (7)	0.10346 (19)
	320	0.09308 (6)	0.2651 (3)	0.10345 (11)
	330	0.09314 (6)	0.2649 (3)	0.10349 (12)
	340	0.09314 (5)	0.2650 (3)	0.10349 (10)
O ₁	100	0.15142 (6)	0.4000 (4)	0.10124 (13)
	200	0.15127 (8)	0.4001 (5)	0.10161 (15)
	300	0.15102 (7)	0.3989 (5)	0.10214 (13)
	320	0.15112 (5)	0.3987 (3)	0.10227 (9)
	330	0.15111 (6)	0.3988 (3)	0.10225 (11)
	340	0.15107 (5)	0.3985 (3)	0.10222 (9)
O ₂	100	0.05416 (7)	0.1293 (4)	0.98697 (13)
	200	0.05436 (6)	0.1299 (5)	0.98764 (15)
	300	0.05424 (8)	0.1300 (5)	0.98804 (13)
	320	0.05441 (5)	0.1298 (3)	0.98799 (9)
	330	0.05457 (5)	0.1300 (3)	0.98818 (10)
	340	0.05448 (5)	0.1303 (3)	0.98812 (9)
O ₃	100	0.07272 (7)	0.2554 (4)	0.20811 (13)
	200	0.07255 (8)	0.2466 (5)	0.20803 (15)
	300	0.07252 (8)	0.2465 (5)	0.20792 (14)
	320	0.07249 (5)	0.2533 (3)	0.20794 (9)
	330	0.07240 (5)	0.2532 (3)	0.20787 (10)
	340	0.07245 (5)	0.2535 (2)	0.20781 (9)
O ₄	100	0.21200 (7)	0.6623 (4)	0.35447 (15)
	200	0.21206 (9)	0.6641 (4)	0.35455 (18)

	300	0.21192 (9)	0.6651 (5)	0.35428 (17)
	320	0.21207 (6)	0.6657 (3)	0.35454 (11)
	330	0.21205 (7)	0.6657 (4)	0.35469 (12)
	340	0.21209 (6)	0.6662 (3)	0.35454 (11)

715

716

717 Table 3: Bond lengths (Å) as a function of temperature and their linear thermal expansion in
718 trona.
719

T (±2) (K)	100	200	300	320	330	340	Thermal Expansion
C ₁ -O ₁	1.283 (2)	1.277 (3)	1.228 (3)	1.2760 (13)	1.2756 (15)	1.2747 (13)	-0.0083 (13)
C ₁ -O ₂	1.320 (2)	1.316 (3)	1.321 (3)	1.3152 (14)	1.3127 (16)	1.3151 (13)	-0.0049 (13)
C ₁ -O ₃	1.263 (2)	1.266 (3)	1.268 (2)	1.2649 (13)	1.2640 (14)	1.2651 (12)	0.0021 (12)
Na ₁ -O ₂ x2	2.4139 (13)	2.4244 (16)	2.4327 (14)	2.4297 (10)	2.4265 (11)	2.4327 (10)	0.0188 (18)
Na ₁ -O ₃ x2	2.3750 (15)	2.3813 (18)	2.3893 (18)	2.3869 (11)	2.3862 (12)	2.3857 (10)	0.0107 (18)
Na ₁ -O ₃ x2	2.4134 (15)	2.4162 (18)	2.4255 (18)	2.4232 (10)	2.4225 (12)	2.4237 (10)	0.0103 (18)
Na ₂ -O ₁	2.6479 (15)	2.6640 (18)	2.6786 (19)	2.6769 (12)	2.6754 (14)	2.6801 (12)	0.0322 (19)
Na ₂ -O ₁	2.3588 (15)	2.3665 (18)	2.3738 (17)	2.3697 (11)	2.3661 (13)	2.3689 (11)	0.0101 (18)
Na ₂ -O ₂	2.4453 (15)	2.4518 (18)	2.4609 (17)	2.4546 (11)	2.4551 (13)	2.4553 (11)	0.0101 (17)
Na ₂ -O ₃	2.3744 (15)	2.3773 (18)	2.3829 (16)	2.3787 (12)	2.3769 (13)	2.3828 (11)	0.0232 (16)
Na ₂ -O ₄	2.3596 (14)	2.3689 (19)	2.382 (2)	2.3838 (12)	2.3839 (14)	2.3854 (12)	0.0238 (19)
Na ₂ -O ₄	2.3707 (14)	2.3779 (18)	2.3881 (18)	2.3875 (11)	2.3860 (13)	2.3880 (11)	0.0173 (18)

720
721
722

723
 724
 725

Table 4: Bond angles of trona as a function of temperature.

T (± 2) (K)	100	200	300	320	330	340
O ₁ -C ₁ -O ₂	115.95 (16)	116.03 (93)	116.23 (13)	116.17 (10)	116.32 (11)	116.21 (9)
O ₁ -C ₁ -O ₃	123.63 (17)	123.8 (2)	123.92 (18)	123.66 (11)	123.71 (12)	123.69 (10)
O ₂ -C ₁ -O ₃	120.42 (17)	120.02 (2)	119.52 (18)	120.16 (10)	119.96 (11)	120.09 (10)
O ₂ -Na ₁ -O ₂	159.43 (8)	159.64 (9)	159.54 (11)	159.49 (6)	159.48 (7)	159.53 (6)
O ₃ -Na ₁ -O ₃ x2	179.12 (5)	179.21 (6)	179.18 (7)	179.18 (4)	179.18 (4)	179.14 (4)
O ₂ -Na ₁ -O ₃ x2	100.48 (5)	100.49 (6)	100.61 (6)	100.60 (3)	100.61 (4)	100.61 (3)
O ₂ -Na ₁ -O ₃ x2	94.26 (4)	94.15 (5)	94.11 (5)	94.16 (3)	94.17 (4)	94.14 (3)
O ₂ -Na ₁ -O ₃ x2	79.46 (4)	79.46 (6)	79.34 (6)	79.34 (3)	79.34 (4)	79.34 (3)
O ₃ -Na ₁ -O ₃ x2	92.47 (5)	92.82 (6)	93.00 (5)	92.98 (3)	93.00 (4)	93.12 (3)
O ₃ -Na ₁ -O ₃	88.41 (7)	87.97 (8)	87.82 (8)	87.84 (5)	87.83 (6)	87.74 (5)
O ₃ -Na ₁ -O ₃	86.65 (7)	86.39 (8)	85.74 (6)	86.20 (5)	86.18 (6)	86.02 (5)
O ₁ -Na ₂ -O ₁	87.18 (5)	87.17 (6)	87.25 (5)	87.24 (4)	87.33 (4)	87.29 (4)
O ₁ -Na ₂ -O ₂	51.17 (4)	50.73 (5)	50.55 (5)	50.54 (3)	50.53 (4)	50.47 (3)
O ₁ -Na ₂ -O ₂	83.91 (5)	84.00 (6)	84.10 (6)	84.19 (4)	84.25 (4)	84.28 (4)
O ₁ -Na ₂ -O ₃	119.33 (6)	119.60 (7)	119.78 (7)	119.96 (4)	119.95 (5)	120.02 (4)
O ₁ -Na ₂ -O ₃	128.06 (5)	127.81 (6)	127.66 (6)	127.66 (4)	127.57 (4)	127.57 (4)
O ₃ -Na ₂ -O ₂	85.74 (5)	85.95 (6)	86.04 (6)	86.11 (4)	86.05 (4)	86.09 (4)
O ₄ -Na ₂ -O ₁	77.16 (5)	76.99 (6)	76.92 (6)	76.87 (4)	76.77 (4)	76.76 (4)
O ₄ -Na ₂ -O ₁	82.95 (5)	82.92 (6)	83.10 (6)	83.07 (4)	83.03 (4)	83.05 (4)
O ₄ -Na ₂ -O ₁	145.10 (6)	145.09 (7)	145.17 (7)	145.00 (4)	144.96 (5)	144.98 (4)
O ₄ -Na ₂ -O ₁	147.85 (6)	147.89 (7)	148.02 (7)	147.85(4)	147.83 (5)	147.86 (4)
O ₄ -Na ₂ -O ₂	108.49 (5)	108.02 (7)	107.76 (7)	107.74(4)	107.68 (5)	107.57 (4)
O ₄ -Na ₂ -O ₂	155.58 (6)	155.98 (7)	156.17 (8)	156.41(4)	156.47 (5)	156.51 (5)
O ₄ -Na ₂ -O ₃	82.90 (5)	82.92 (6)	83.10 (6)	83.19(4)	83.29 (5)	83.25 (4)
O ₄ -Na ₂ -O ₃	94.53 (5)	94.36 (6)	94.10 (6)	94.07(4)	94.12 (5)	94.06 (4)
O ₄ -Na ₂ -O ₄	93.96 (5)	94.12 (7)	94.15 (6)	93.97(4)	93.99 (5)	94.04 (4)

726
 727

728

729 Table 5. Raman and infrared modes observed at room temperature and pressure, pressure
 730 dependences of peak positions, and calculated mode Grüneisen parameters of trona (some
 731 assignments based on Novak et al. (1963), others based on this study).
 732

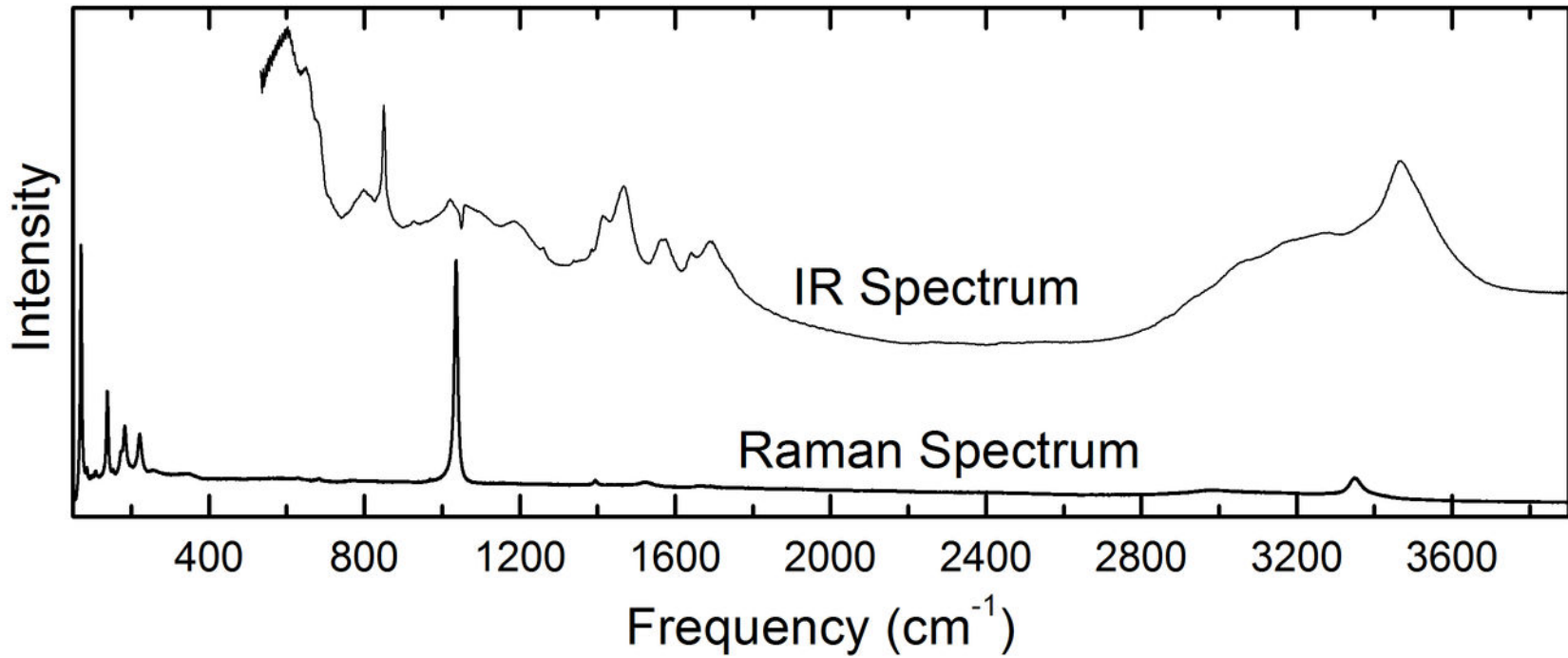
ν_{0i} (cm^{-1})	Assignment	$(d\nu_{0i}/dP)$ to 7GPa ($\text{cm}^{-1}/\text{GPa}$)	γ_i
71	Na-O-Na (R)	1.78 (± 0.24)	0.90
100	Na-O-Na (R)	2.06 (± 0.09)	0.74
108	Na-O (R)	6.03 (± 0.48)	2.01
139	Na-O (R)	4.34 (± 0.31)	1.12
155	Na-O (R)	4.74 (± 0.37)	1.10
172	Na-O (R)	4.69 (± 0.36)	0.98
684	ν_4 (IR)	4.14 (± 0.25)	0.22
699	ν_4 (R)	4.79 (± 0.36)	0.25
710	ν_4 (IR)	5.66 (0.40)	0.29
806	H ₂ O Lib (IR)	6.21 (± 0.72)	0.28
850	ν_2 (IR)	-1.01 (± 0.10)	-0.04
1051	Transmission Window (IR)	5.89 (± 0.35)	0.20
1060	ν_1 (R)	5.37 (± 0.25)	0.18
1461	ν_3 (IR)	3.80 (± 0.30)	0.09
1557	1 st Overtone of 806 (IR)	11.60 (± 1.0)	0.26
1698	O-H...O transition? Combination? (IR)	1.58 (± 0.90)	0.03
1749	O-H...O transition? Combination? (IR)	5.95 (± 0.73)	0.12
3049	H ₂ O (IR)	-7.98 (± 0.26)	-0.09
3449	H ₂ O (IR)	-5.46 (± 0.76)	-0.06
3530	H ₂ O (IR)	-6.10 (± 1.34)	-0.06

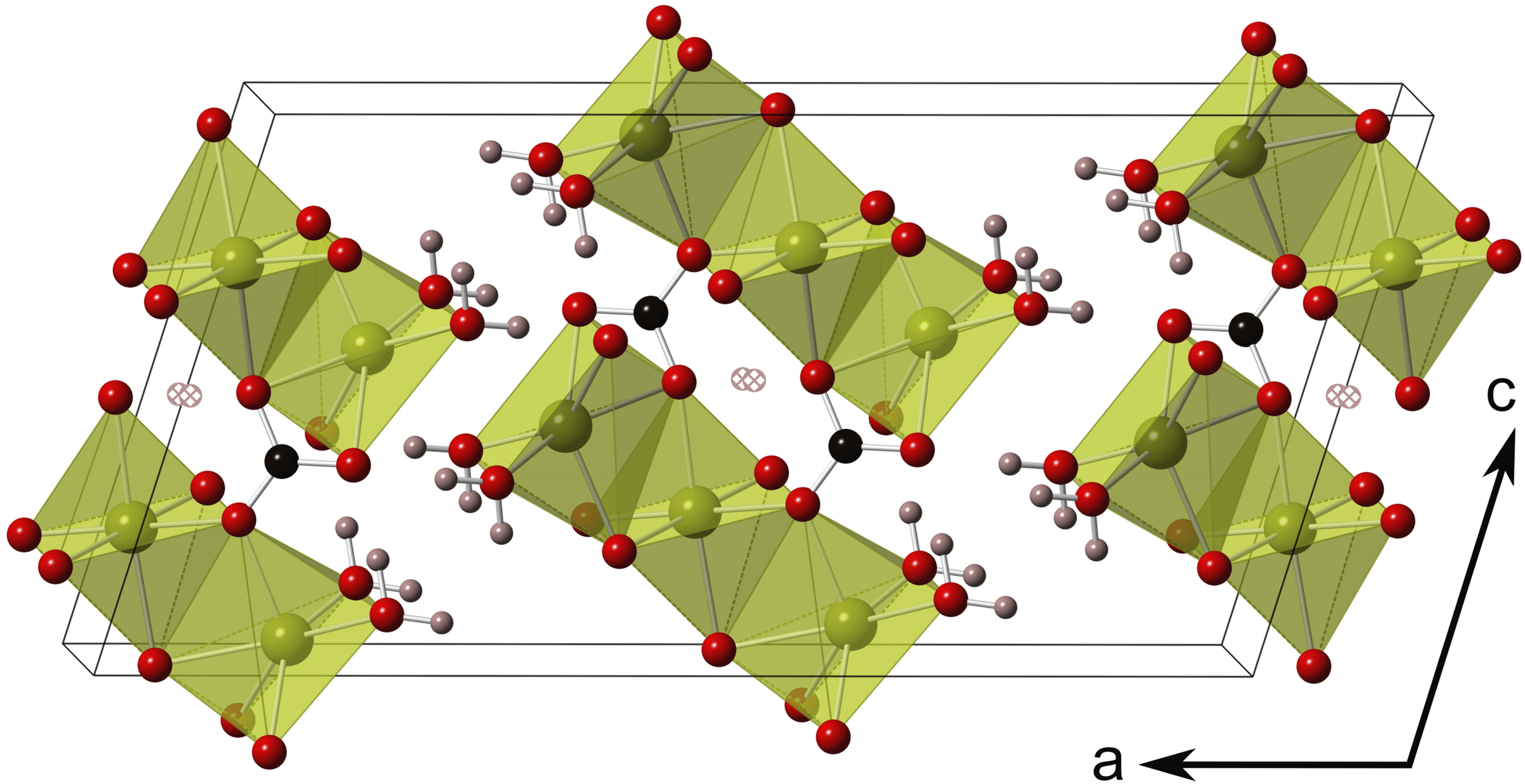
733

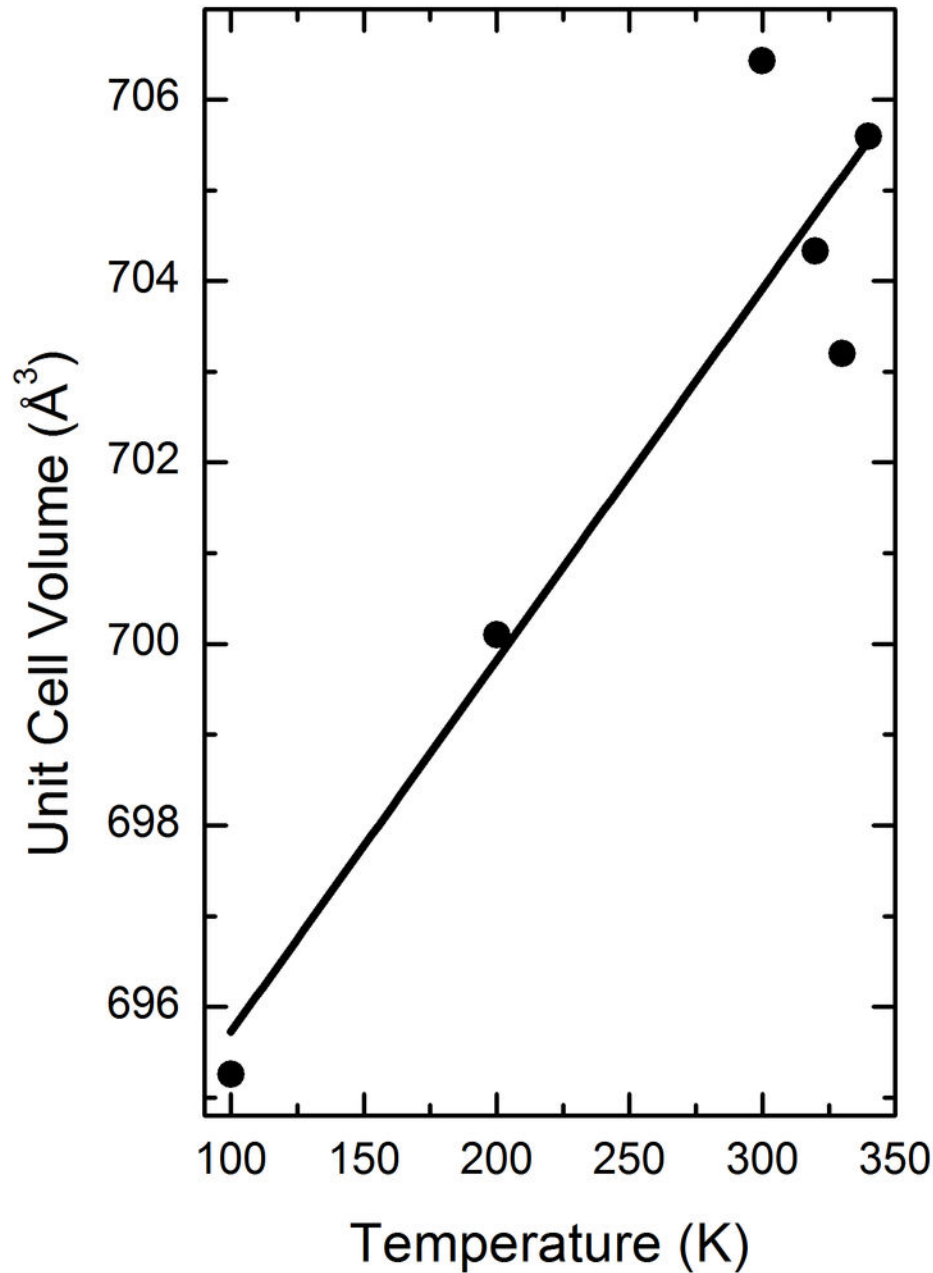
734

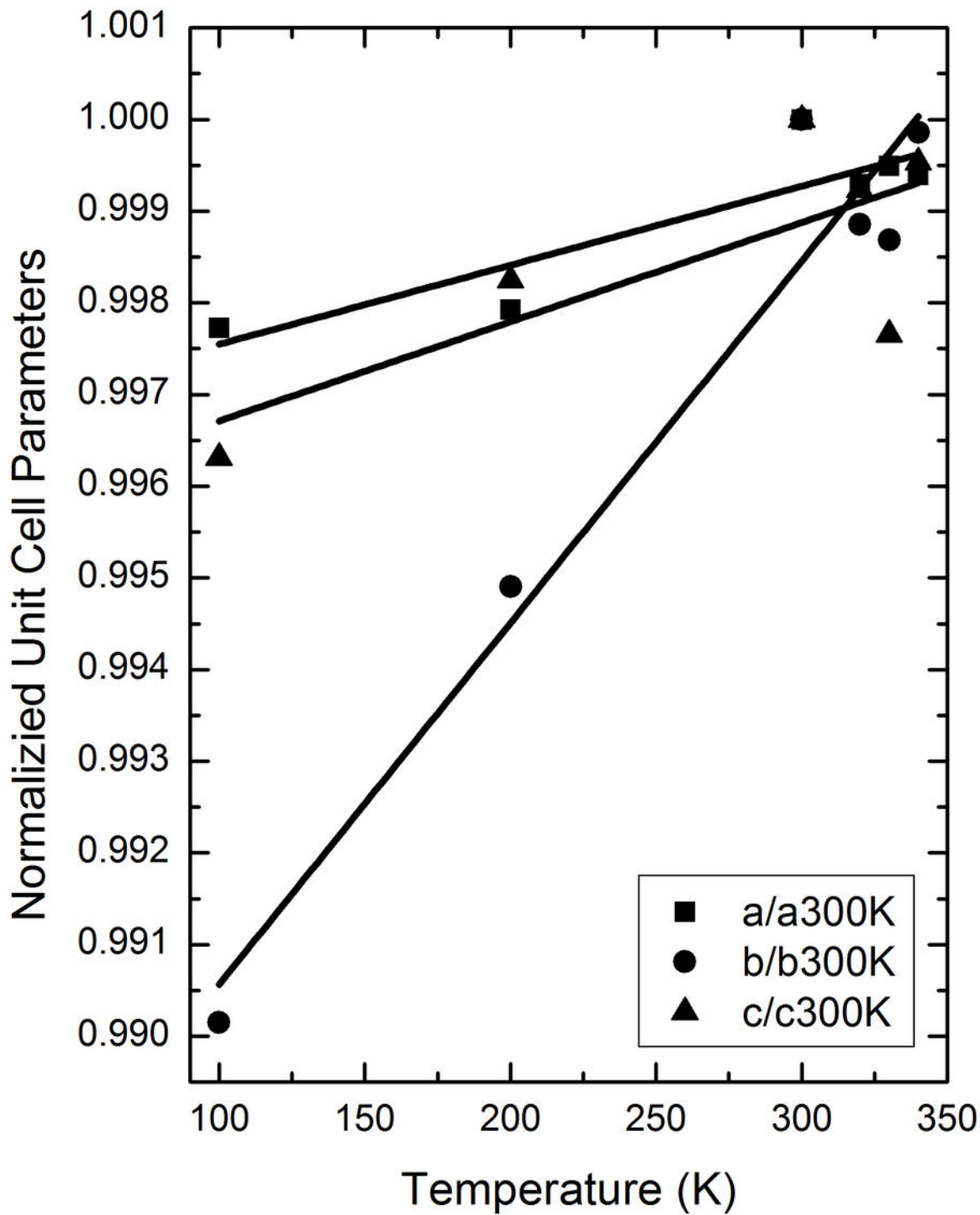
735

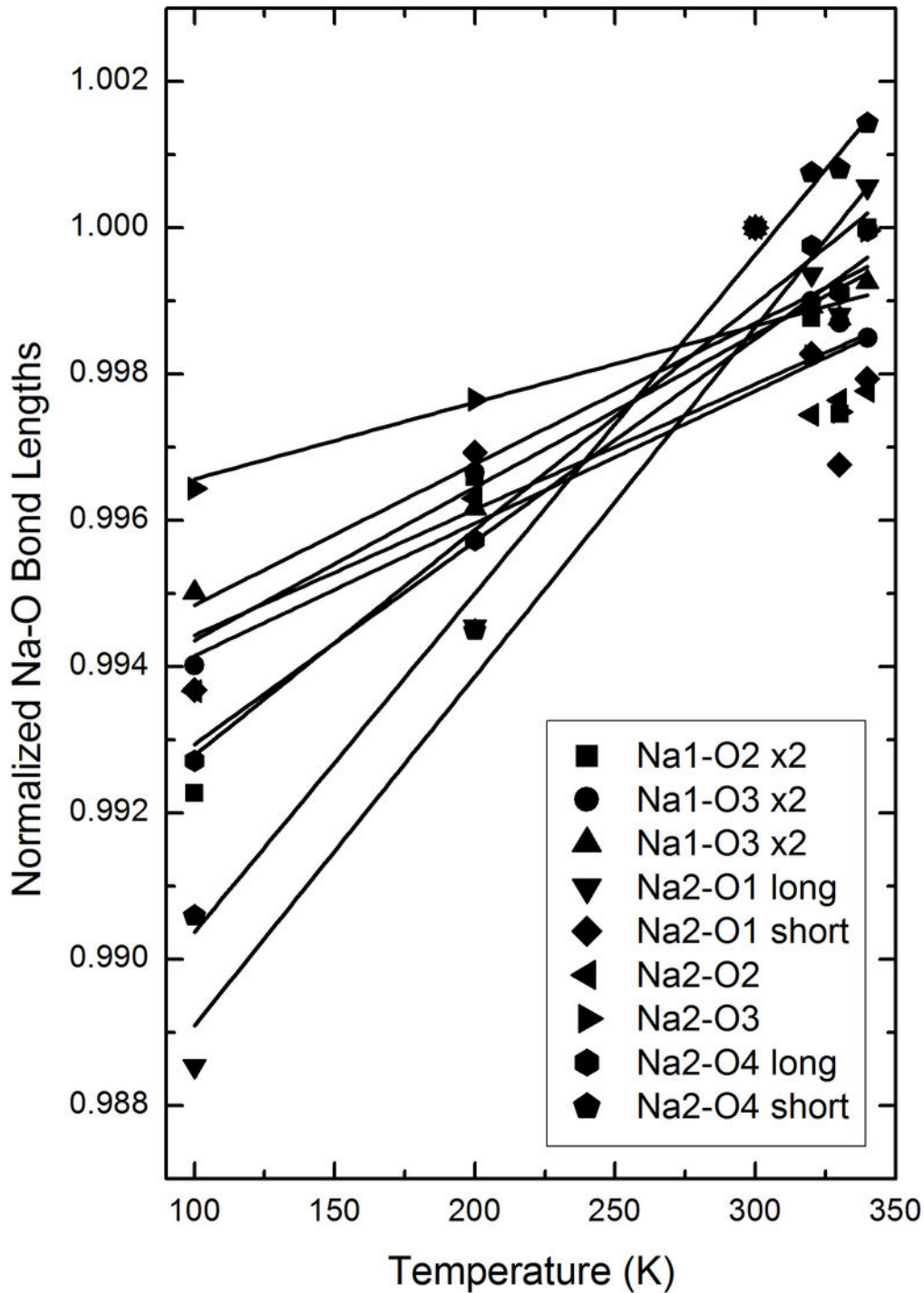
736

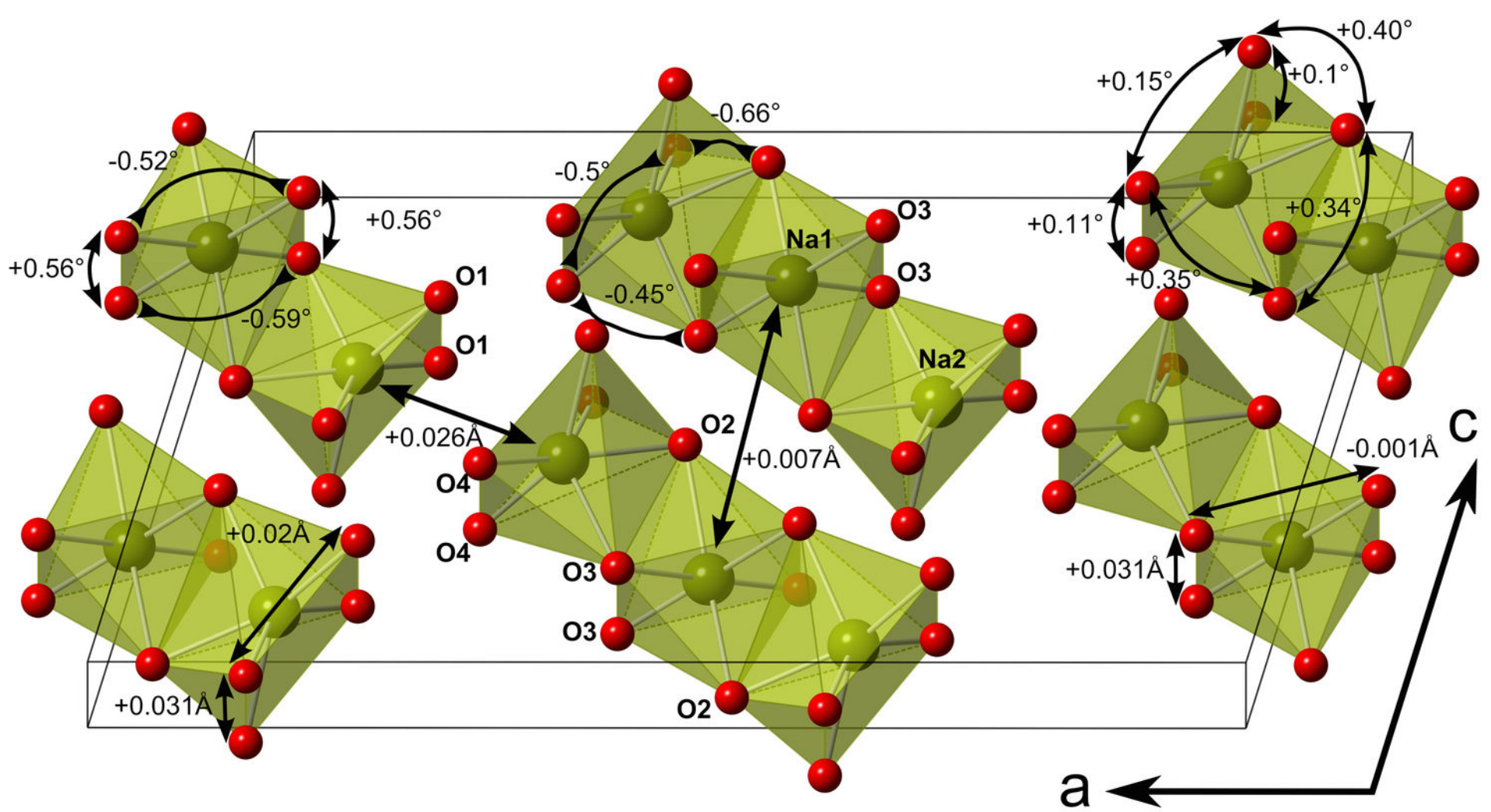




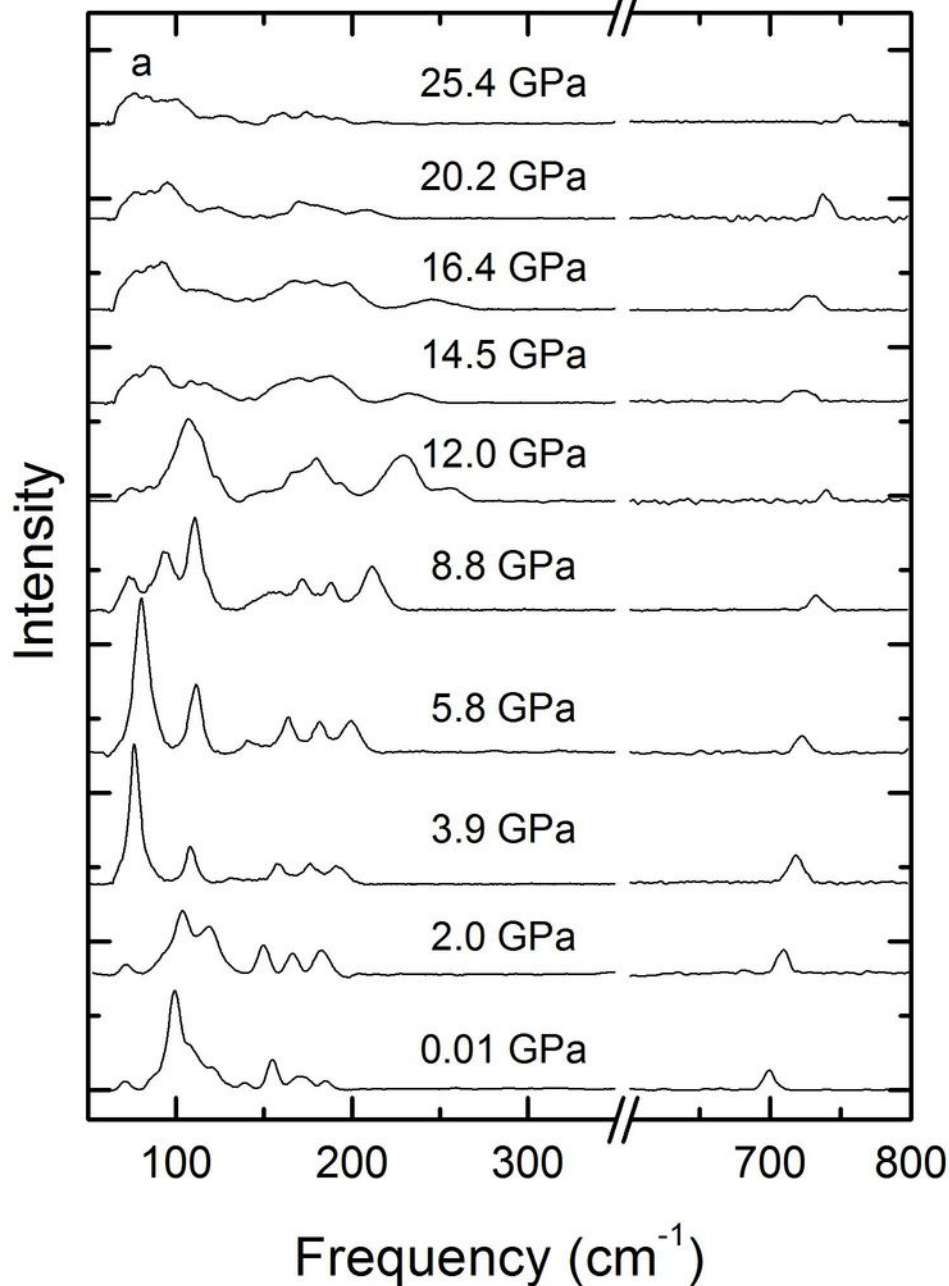




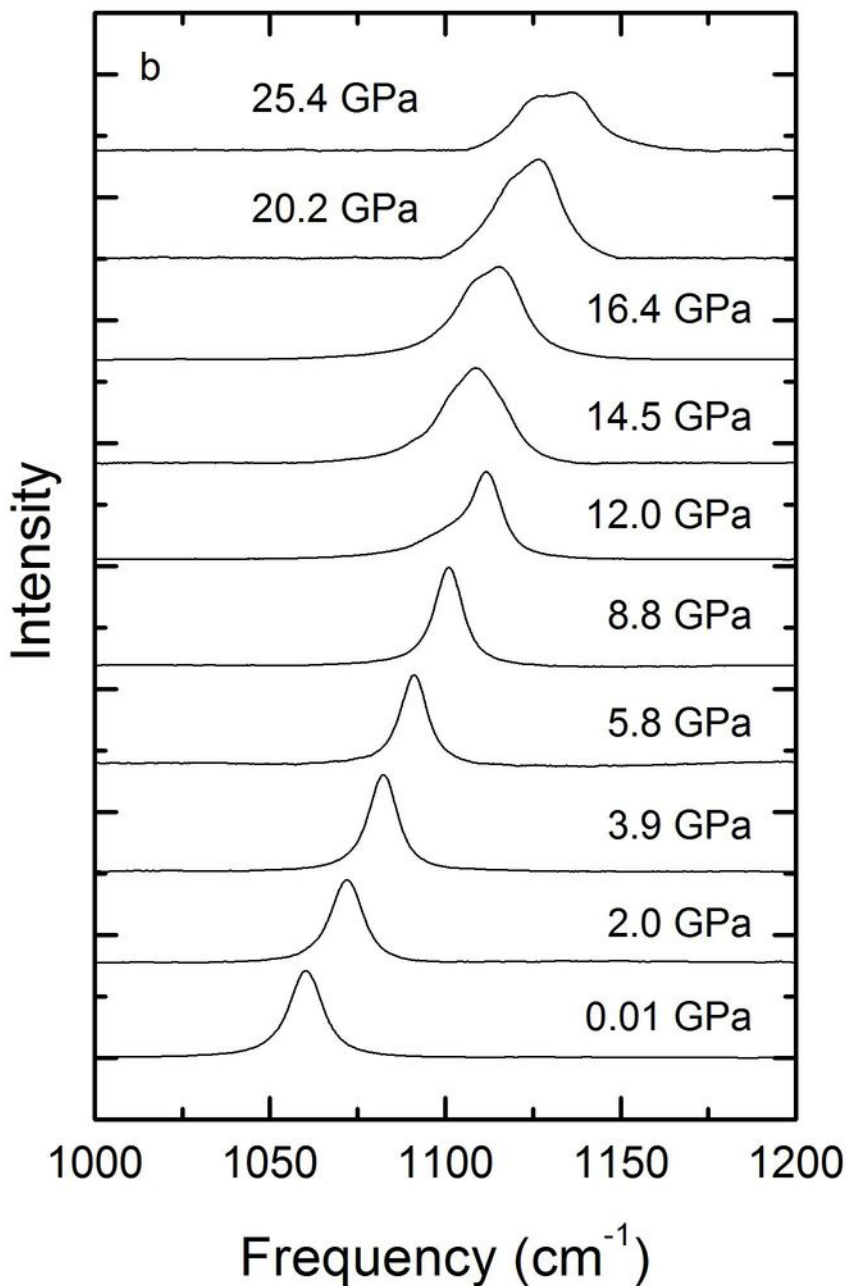




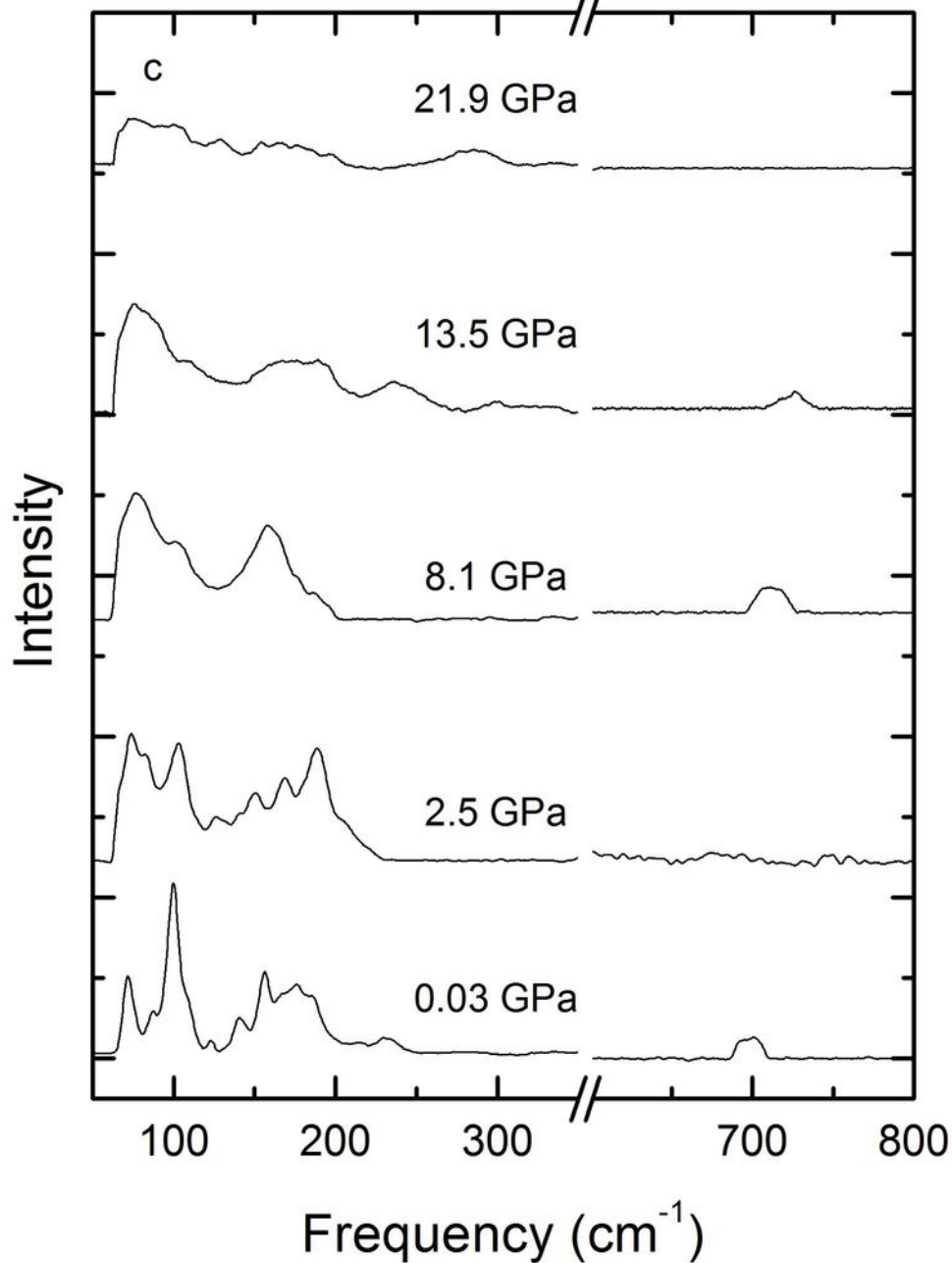
Compression



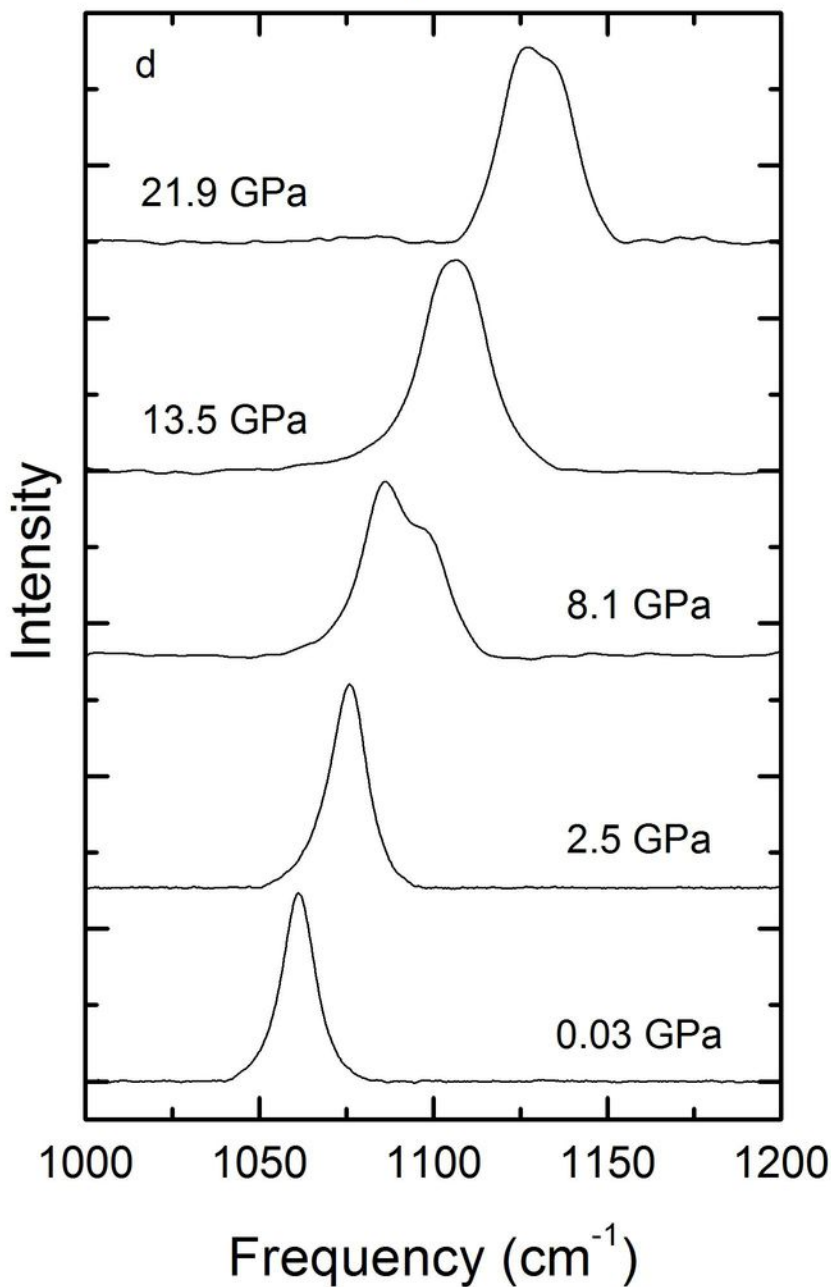
Compression

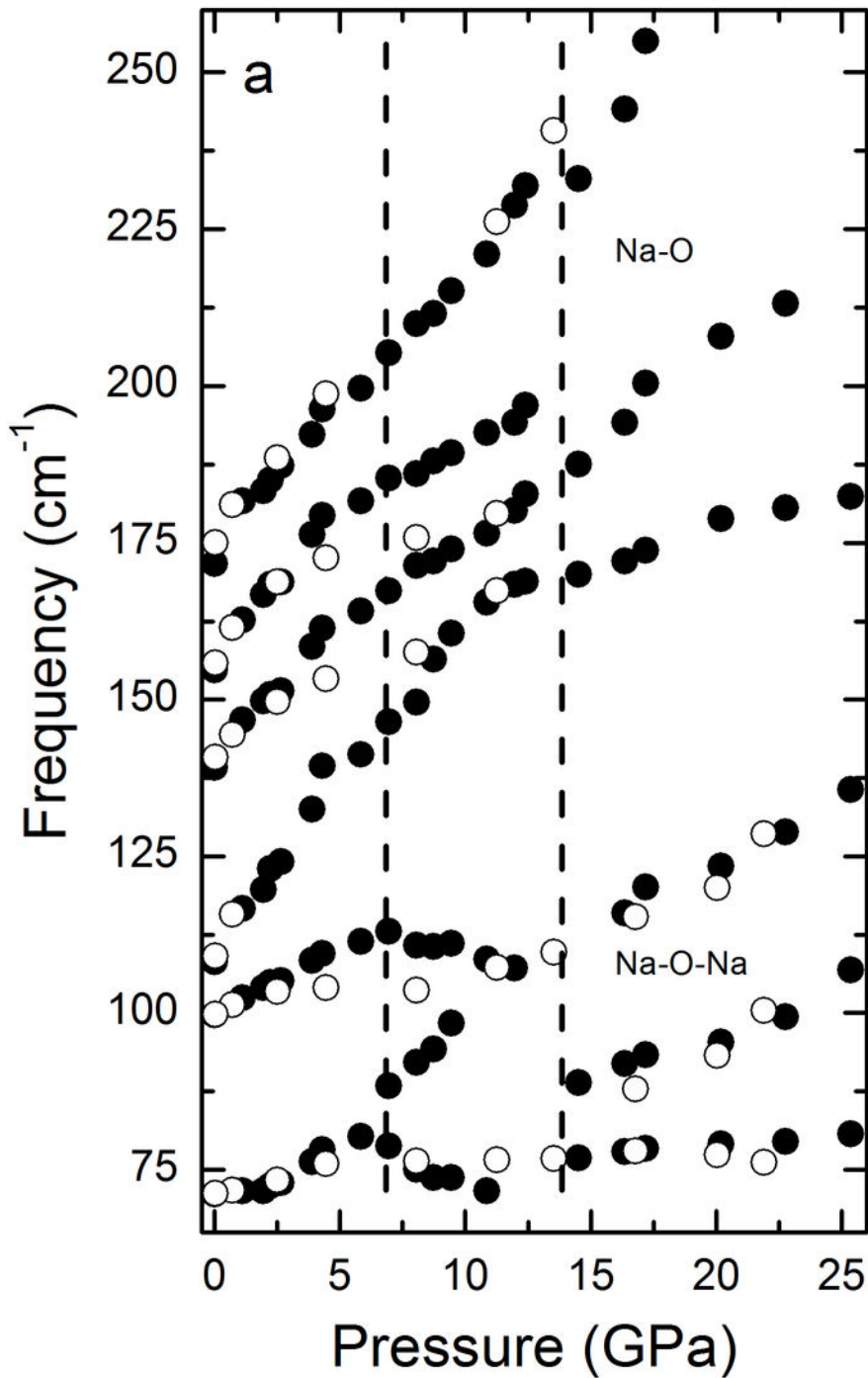


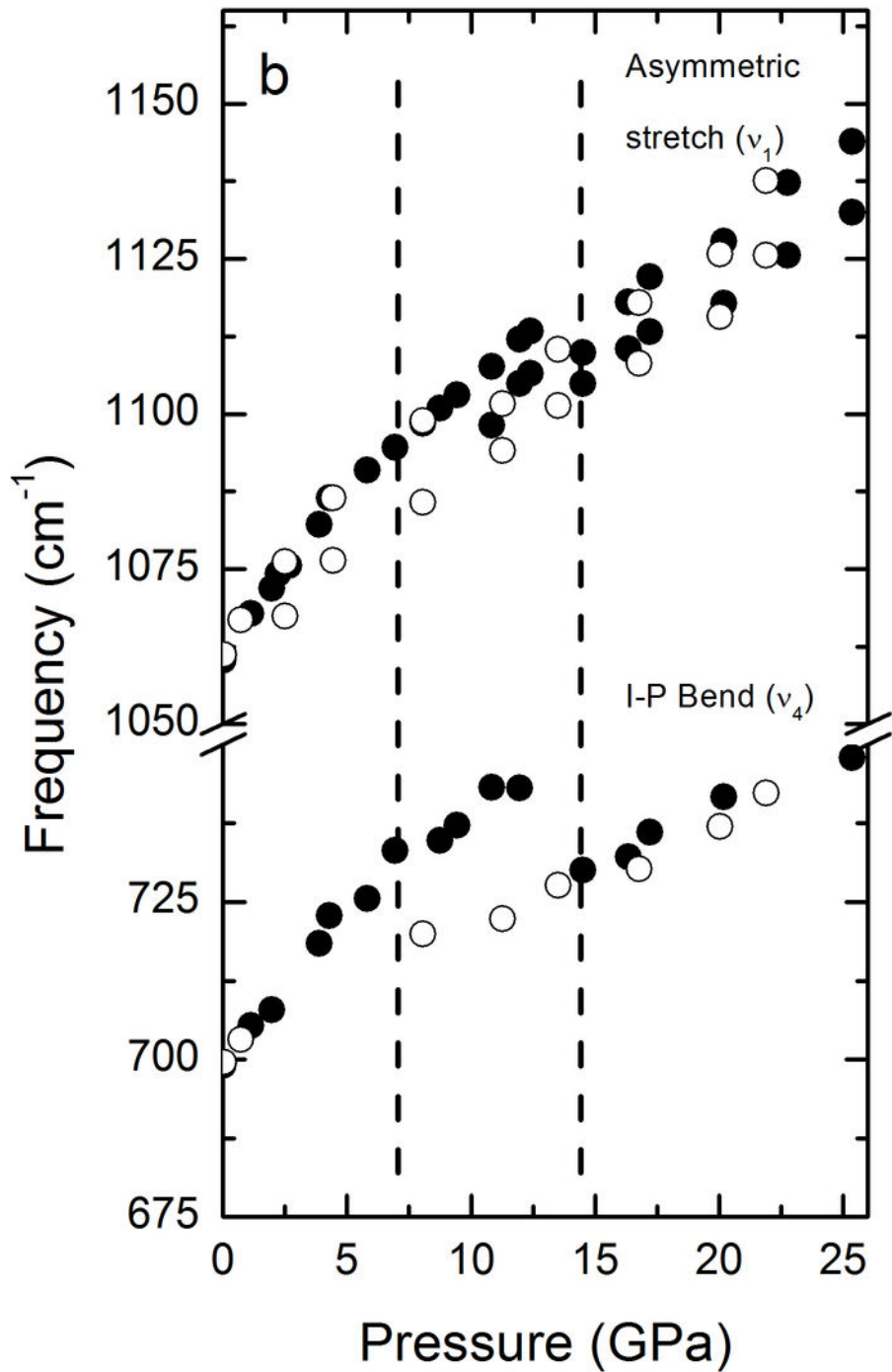
Decompression



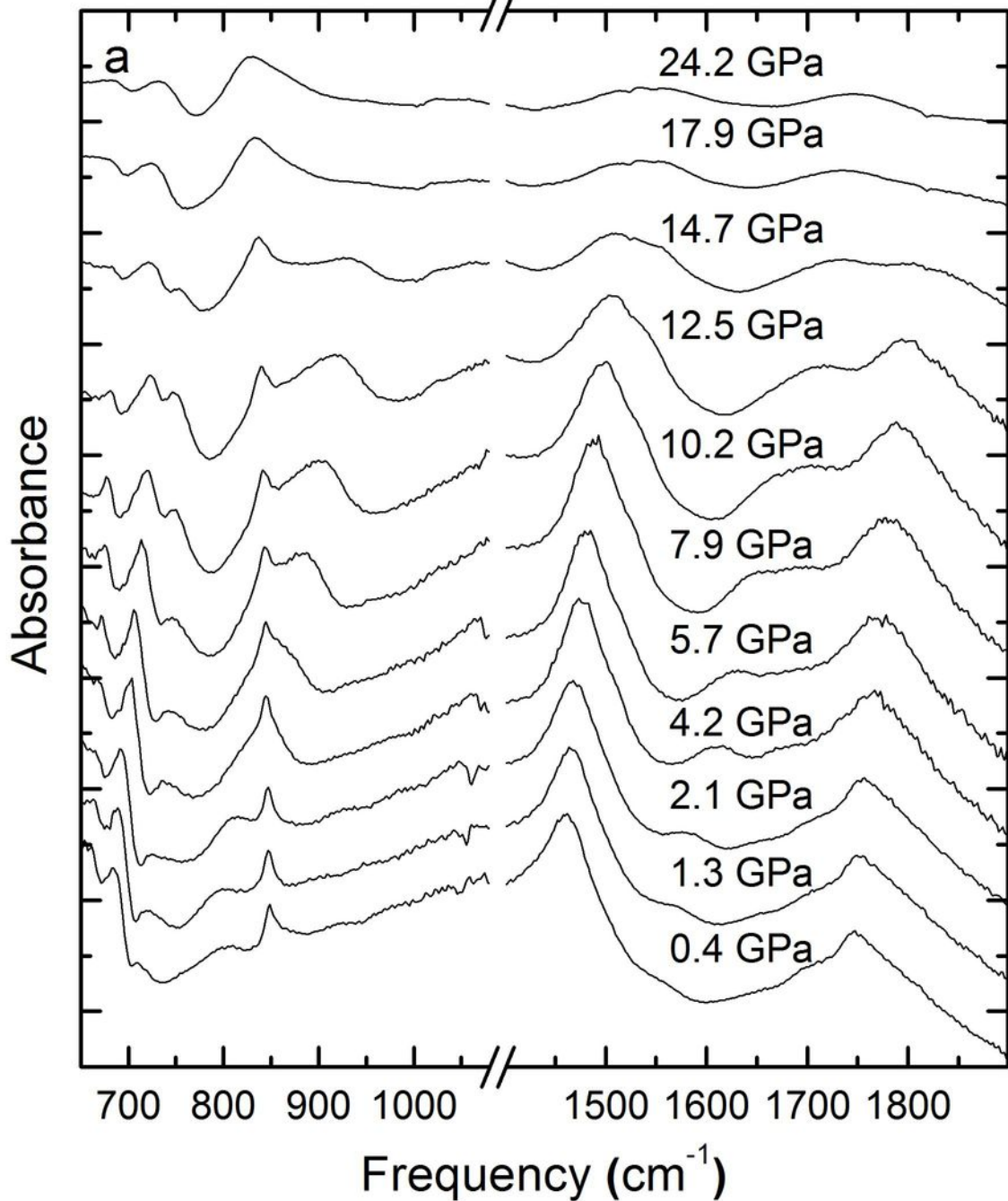
Decompression



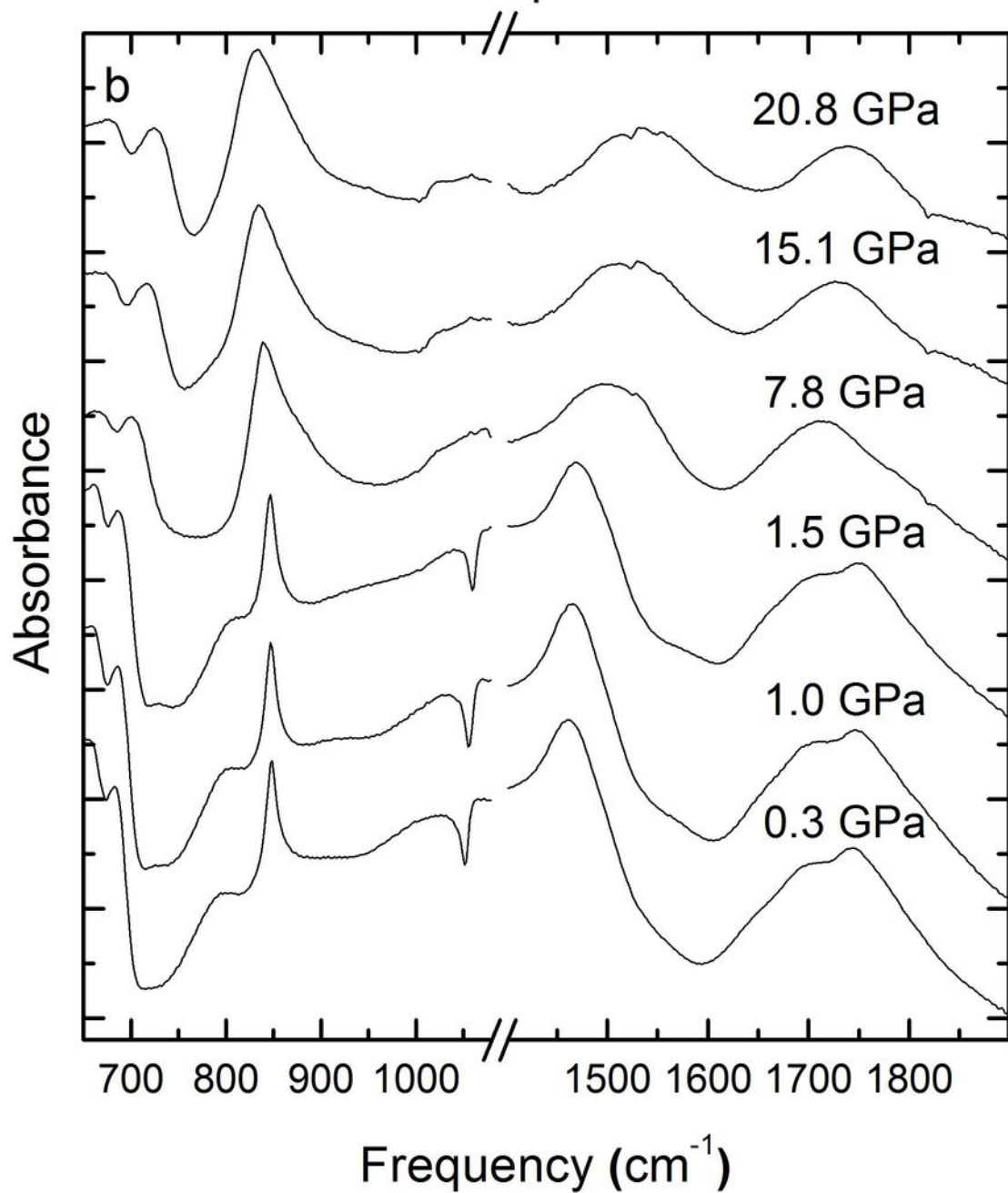




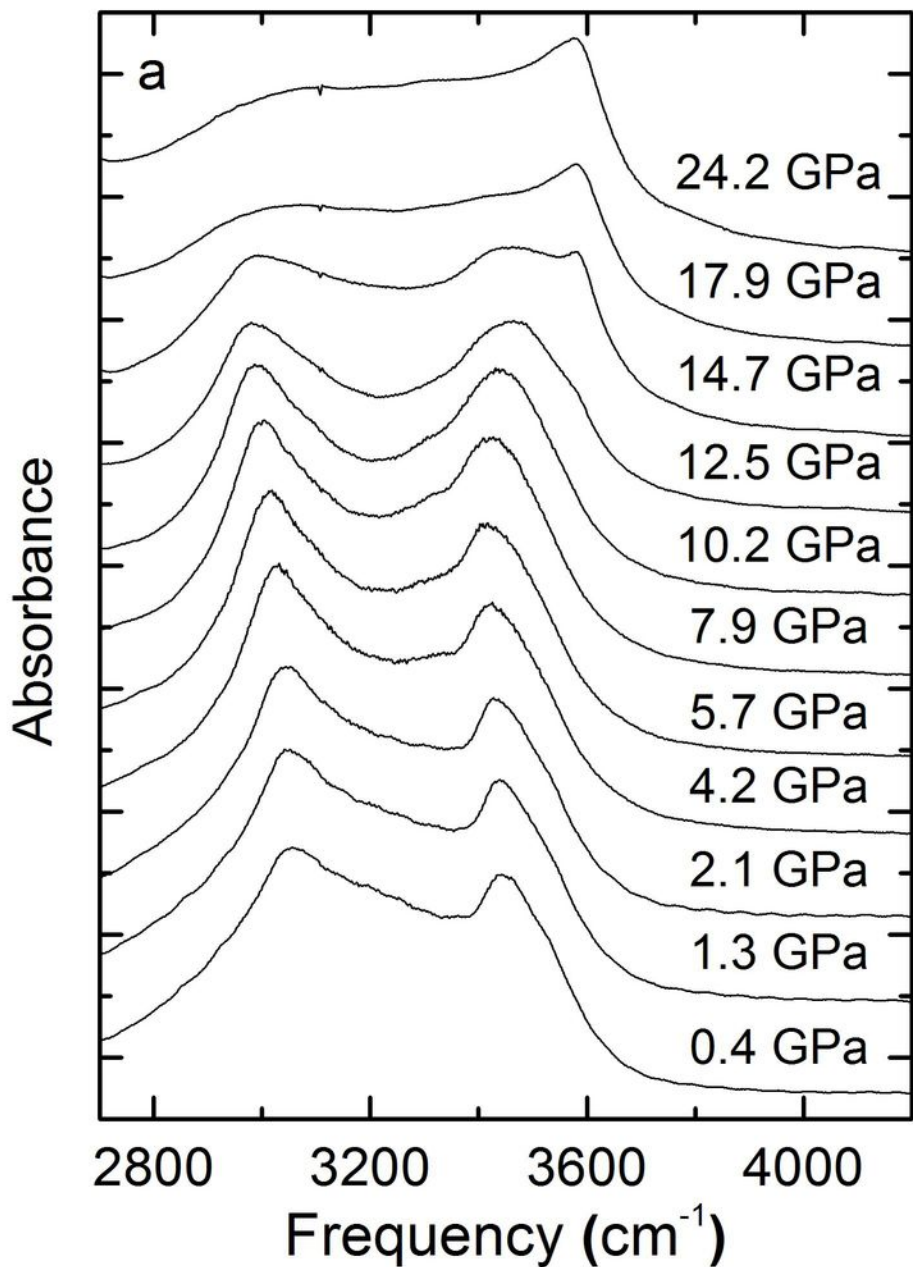
Compression



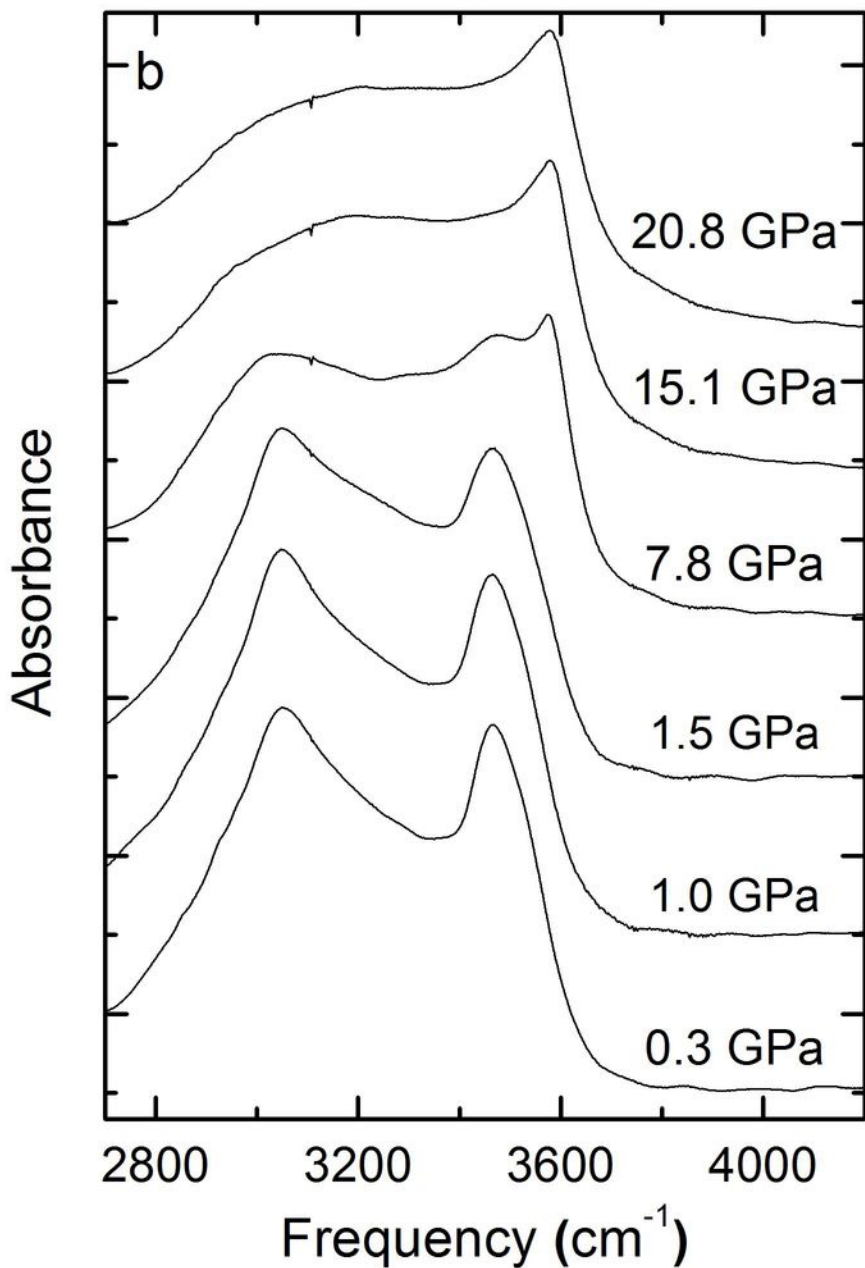
Decompression

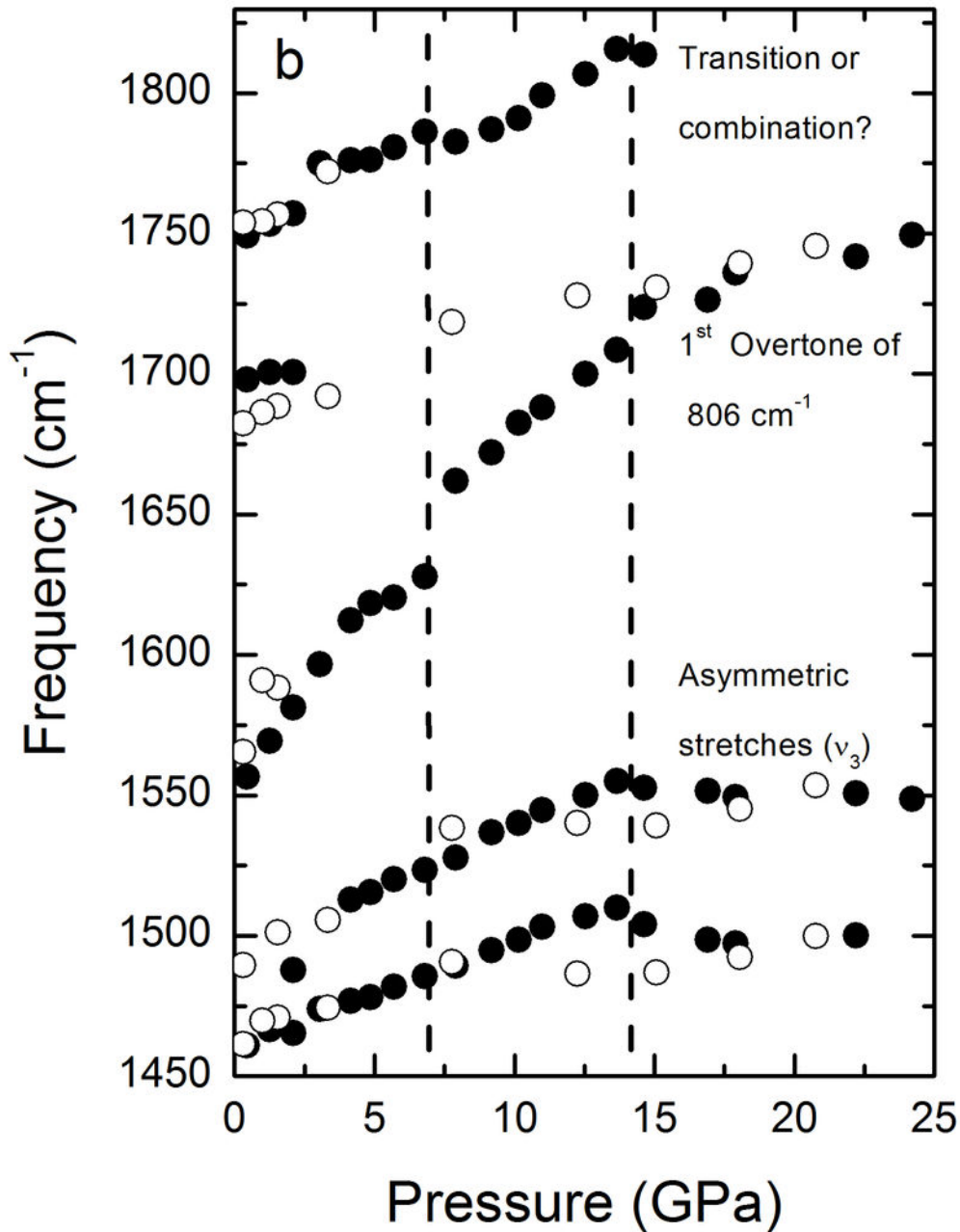


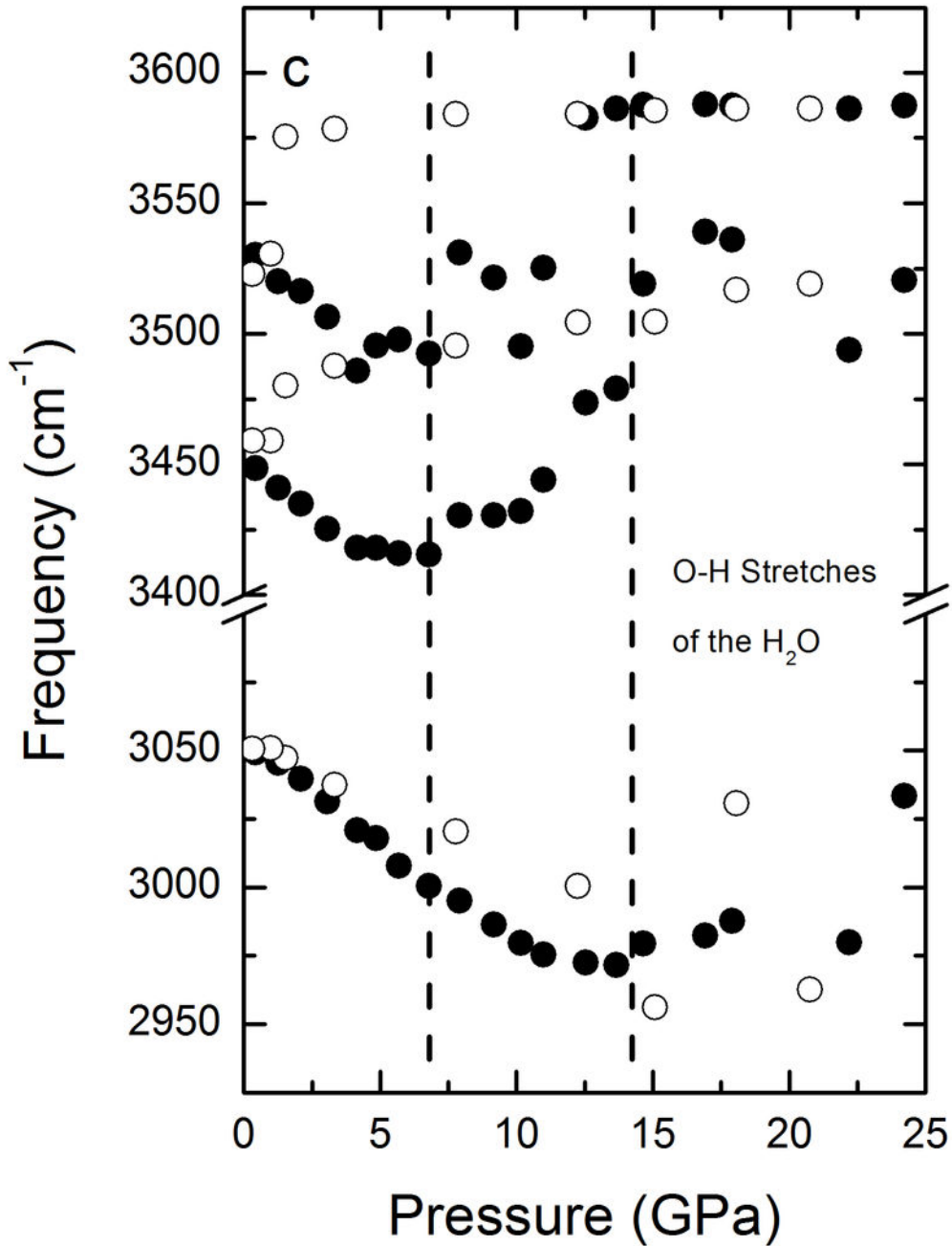
Compression



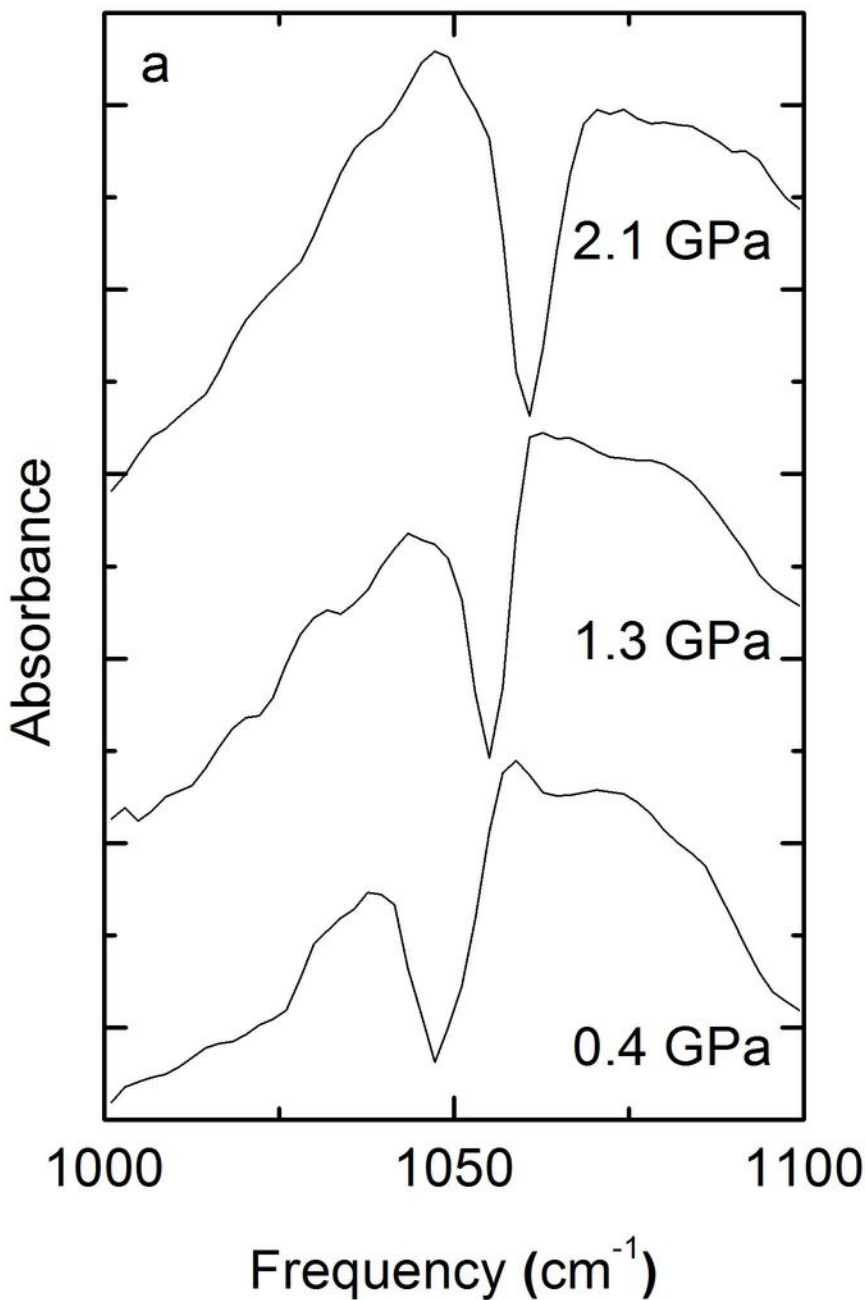
Decompression







Compression



Decompression

